Numerical Study of Turbulent Wake of Offshore Wind Turbines and Retention Time of Larval Dispersion

Souha Ajmi, Martial Boutet, Anne-Claire Bennis, Jean-Claude Dauvin, Jean-Philippe Pezy

Journal of
Marine Science and Engineering

MDPI

Article

Numerical Study of Turbulent Wake of Offshore Wind Turbines and Retention Time of Larval Dispersion

Souha Ajmi *, Martial Boutet, Anne-Claire Bennis, Jean-Claude Dauvin and Jean-Philippe Pezy

Morphodynamique Continentale et Côtière (UMR CNRS 6143), Université de Caen (Campus 1), CEDEX, 14000 Caen, France; martial.boutet@unicaen.fr (M.B.); anne-claire.bennis@unicaen.fr (A.-C.B.); jean-claude.dauvin@unicaen.fr (J.-C.D.); jean-philippe.pezy@unicaen.fr (J.-P.P.)
* Correspondence: souha.ajmi@unicaen.fr

Abstract: Offshore Wind Farm (OWF) foundations are considered to have a potential impact on the larval dispersion of benthic species. This study focused on OWFs' impacts on larval dispersion, considering factors such as the foundation type, flow velocity, flow direction, and release type using numerical modelling. At the scale of monopile and gravity-based foundations, a combination of two numerical models was used: the Eulerian model (OpenFOAM), solving the 3D Navier–Stokes equations for computing the hydrodynamics, and the Lagrangian model (Ichthyop), solving the advection–diffusion equation for the larval dispersion simulations. The validation model tests were evaluated with experimental data as a first step of the study. Accurate results were achieved, yielding a Turbulent Kinetic Energy (TKE) Root-Mean-Squared Error (RMSE) in the range of 6.82–8.27 $\times$ 10^{-5} kg/m $\cdot$ s^2 within the refined mesh, with a coefficient of determination (R^2) approaching unity. For the second phase, more-realistic simulations were modelled. Those simulations demonstrated turbulent wakes downstream of the foundations and horseshoe vortex formations near the bottom. A larval dispersion was simulated using passive particles' motion. Vertical flumes in the wake with particles experiencing both upward and downward motions, impacting the fall velocities of the particles, were observed. The influence of gravity-based foundations might lead to a stepping-stone effect with a retention time of up to 9 min, potentially allowing the settlement of competent larvae. In a similar geometry with an angular spring tide velocity, 0.4% of particles were trapped.

Keywords: environmental fluid mechanics; marine renewable energy; larval dispersal; Eulerian–Lagrangian coupling

Citation: Ajmi, S.; Boutet, M.; Bennis, A.-C.; Dauvin, J.-C.; Pezy, J.-P. Numerical Study of Turbulent Wake of Offshore Wind Turbines and Retention Time of Larval Dispersion. *J. Mar. Sci. Eng.* **2023**, *11*, 2152. https://doi.org/10.3390/jmse11112152

Academic Editor: Dong-Sheng Jeng

Received: 20 October 2023
Revised: 7 November 2023
Accepted: 8 November 2023
Published: 14 Novemebr 2023

1. Introduction

The story of the wind farm industry started on land; however, its marine sector is progressing at a faster pace in the world, achieving higher growth over the years [1,2]. This progress may be due to some factors including the sea's distance from residential areas, which raise concerns about pollution in all its forms in their surroundings, and the lack of a means of transportation compared to land. For the EU, the first goal of renewable energy development is to achieve carbon neutrality. To reach this goal, the coastal marine zones present one of the natural components for renewable energies in various forms, allowing the production of electricity from different resources in the marine environment. The wind intensity is stronger on sea than on land. Hence, France has set a target of 40GW of offshore wind capacity by 2050. Normandy takes the lead in OWF projects (Figure 1) with five OWFs planned, including two OWFs that are currently under construction, since 2021 (Courseulles-Sur-Mer and Fécamp). The Courseulles-Sur-Mer OWF set out to have an operational capacity of 448MW with 64 turbines. Also, Fécamp is a 497MW OWF project containing 71 turbines. Each turbine will be placed on a specific foundation type. For these bottom-mounted turbines, four types of structures, depending on the depth and soil

properties, have been chosen by the companies (Figure 2). In our study, only two of these four foundations were considered. On the one hand, the monopile foundation used in the Courseulles-Sur-Mer OWF was studied by [3,4] considering the sandy and gravely seabed and a water depth between 20 and 30 m above the sea bed (e.g., [5,6]). On the other hand, the gravity-based foundation in the Fécamp OWF has been investigated. As mentioned in Figure 2, a gravity-based foundation will be built for a water depth between 30 and 39 m above the sea bed and the flat gravely bottom. The two OWFs are located in the extended Bay of Seine, an area that represents good wind resourceswith a wind speed >15 m/s [7]. OWFs' foundations are situated in coastal seas, presenting hydrodynamic changes, which have led to several studies on the fluid and structure interactions. It is worth noting that there is also a wide mix of impacts [8] such as the impact on sediments/the mobility of sediments [9] or on the intensity of the wind [10]. Monopiles are applied in the majority of industrial offshore foundations. The flow behaviour around this type of foundation has been experimented with at different Reynolds numbers in previous studies, like [11–13]. Those research works presented a basis for other studies, like [14,15], as well as [16,17], who investigated the production of a horseshoe vortex around the structure and near the bottom. The authors of [18] studied the three-dimensional flow in the wake according to the Reynolds number and the generation of the von Kármán vortex streets downstream of the pile. The authors of [19] explained the flow behaviour and vortex shedding formation in the presence of a vertical cylinder. To understand the different physical phenomena, numerical modelling is useful to avoid costly prototypes for experimentation and to learn how to reproduce realistic physical processes, like [20], in the case of a cylindrical structure. For turbulent flow conditions, Direct Numerical Simulations (DNSs) are used to produce the physical quantities of the flow as described by the Navier–Stokes equations [21]. This type of Computational Fluid Dynamics (CFD) simulation requests higher computational resources, so having a higher cost. A solution then consists of solving the Navier–Stokes equations by using the averaged parameters as the Reynolds-Averaged Navier–Stokes (RANS) equations. Many previous studies used the RANS equations with a two-equation turbulence model, like [22], who applied k-ω. The authors of [23] investigated the Shear Stress Transport (SST) turbulence model based on the k-ω formulation, while [24] applied k-ϵ as a turbulence model for Reynolds numbers between 10^4 and 10^7. The recent study of [25] confirmed that the RANS k-ω SST turbulence model is the best way to generate the same results as the experimental and computationally expensive 3D model results.

Our study pursued the previous ones by applying the RANS k-ω SST turbulence model at a local scale, which contains one to two foundations per configuration, using OpenFOAM as the CFD numerical modelling and coupling it with a Lagrangian model. Depending on the flow conditions, turbulence may influence the transport of particles that colonisearound the structure of the wind turbine. As a result, an increase in particle dispersion near the structure can be visualised. The extended Bay of Seine, which was chosen for this study, contains a great biodiversity of native or non-native hard substrate benthic species. The dispersal of larvae is an important phenomenon for the survival of the populations of species with a bentho-pelagic biological cycle [26]. During the planktonic larval phase, close to the foundations, the larvae's dispersion will be impacted [27], as discussed by [8,28]. Various studies have investigated the potential influence of OWFs on benthic species using coupled hydrodynamic and biological models [29–31]. Field measurements also served this purpose in [32]. They observed that the presence of structures increased the vertical mixing and species production as a consequence of the nutriment transport rise. In this work, the species were considered as passive particles, therefore without biological forcing [33]. Furthermore, this study aimed to simulate the flow around two types of foundations used for Fécamp (gravity-based structure) and Courseulles-Sur-Mer (monopile structure). It assessed their impacts on the larvae's dispersion at a local scale around the OWF foundations.

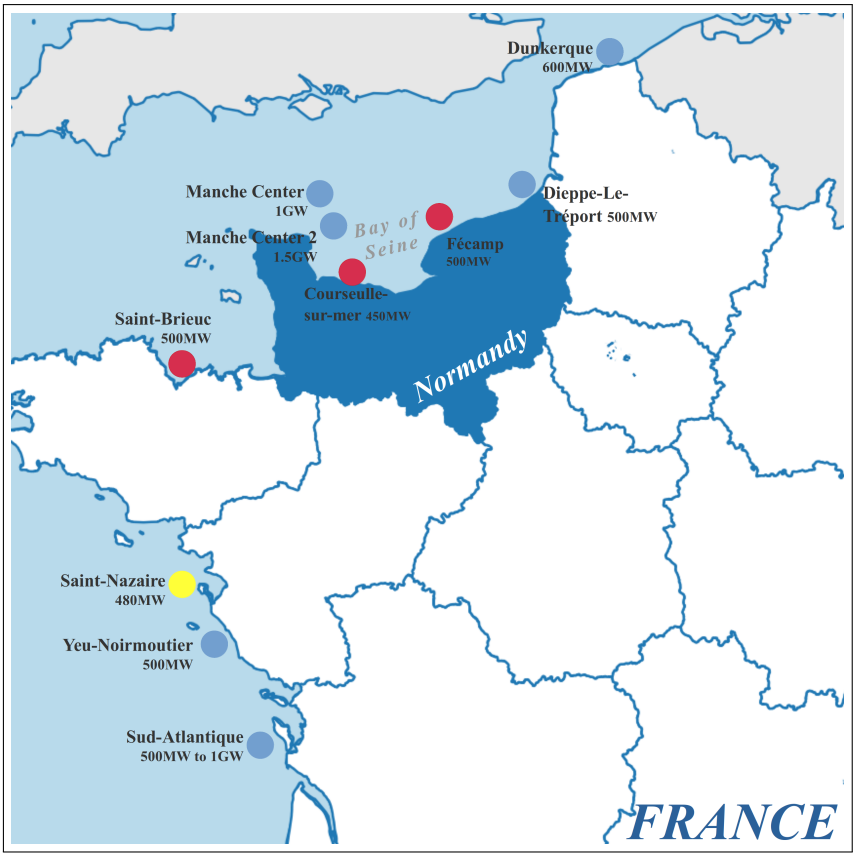

Figure 1. French future OWFs with fixed bottom turbines: in operation (yellow areas), under construction (red areas), and development phase (blue areas).

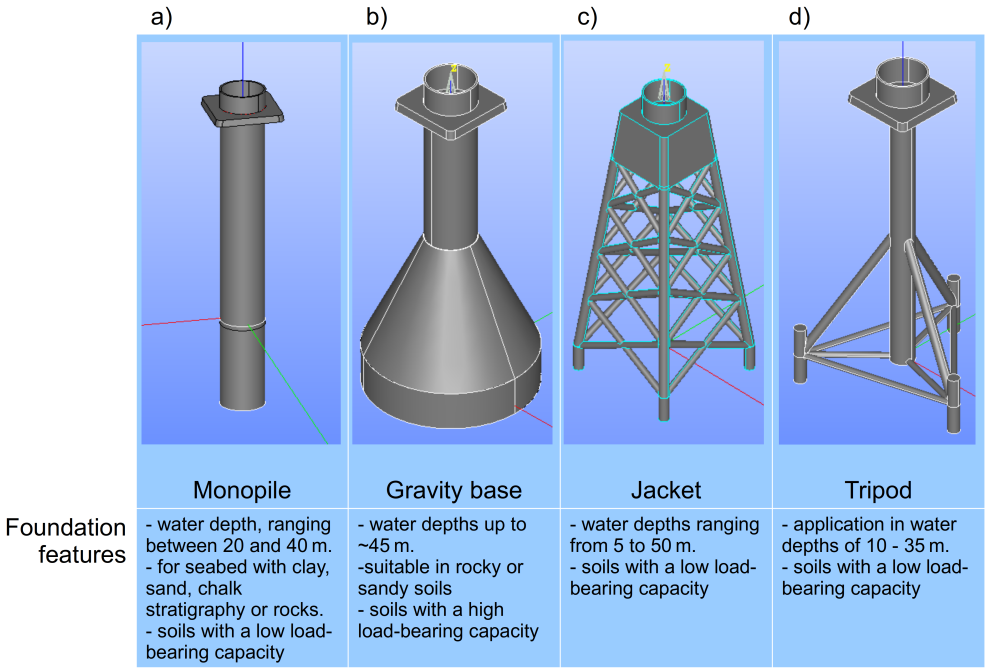

Figure 2. Diverse foundation types ((**a**) Monopile, (**b**) Gravity-Based, (**c**) Jacket, and (**d**) Tripod) and their features regarding suitable water depths and favorable soil types for installation [34,35].

The paper's structure is outlined as follows: Following the Introduction in Section 1, Section 2 provides an overview of the hydrodynamic model and the Lagrangian model. This includes the presentation of their governing equations, as well as the initial and boundary

conditions. The coupling procedure is elaborated upon at the end of Section 2. Moving on to Section 3, the focus shifts to the domain geometry, the mesh, and the results related to a laboratory test case from [36]. In Section 4, the domain geometry, mesh details, and simulation results for real test cases involving either one or two foundations are presented under varying hydrodynamic conditions. The related conclusions are detailed in Section 5.

2. Model Description

To assess the influence of OWF foundations on larval dispersal, two distinct numerical models were employed, and their descriptions are outlined in the subsequent sections. Furthermore, the coupling procedure employed is elaborated in this section. Each model is accompanied by a comprehensive presentation of its respective initial and boundary conditions.

2.1. Hydrodynamic Model

2.1.1. Governing Equations

As a hydrodynamic model, Open Field Operation and Manipulation (OpenFOAM) [37] is applied to reproduce fluid–foundation effects. OpenFOAM is a CFD numerical model that can simulate fluid dynamics at a local scale around one or several OWF foundations. The regional scale containing the whole OWF foundations requires many computational resources and time, which OpenFOAM does not support. Here, the turbulence induced by the fluid–foundation interactions is modellised using the Reynolds-Averaged Navier–Stokes (RANS) approach. OpenFOAM using the RANS approach solves the averaged three-dimensional Navier–Stokes equations, respectively, the continuity (Equation (1)) and momentum equations (Equation (2)):

$$\begin{cases} \nabla \cdot \vec{u} = 0, & (1) \\ \rho \dfrac{\partial \vec{u}}{\partial t} = -\nabla p + \mu \nabla^2 \vec{u} + \rho \vec{g}, & (2) \end{cases}$$

where $\vec{u}$ represents the flow velocity, p is the normalised pressure, and $\vec{g}$ is the gravity acceleration. ρ and μ are the density and dynamic viscosity of the fluid. The solver pimpleFOAM of OpenFOAM is used to solve Equations (1) and (2). It is a transient solver applicable for incompressible and turbulent flow on a mesh. The pimpleFOAM solver is based on the PIMPLE algorithm, which combines the Pressure Implicit with Splitting of Operator (PISO) algorithm proposed by [38] and the Semi-Implicit Method for Pressure-Linked Equations (SIMPLE) algorithm of [39]. To sum up, PIMPLE iterates the solution of pressure–velocity coupling within a time step. This algorithm ends its loop by reaching a static number of iterations or a residual limit [40]. The turbulence downstream of the structure is simulated using the k-ω Shear Stress Transport (SST) already implemented in OpenFOAM [23]. The k-ω SST is a RANS model solving two evolution equations for the turbulent kinetic energy k (Equation (3)) and for the modified turbulent dissipation ω (Equation (4)) as follows [41]:

$$\begin{cases} \dfrac{\partial \rho k}{\partial t} + \nabla(\rho u k) = \nabla(\Gamma_k \nabla k) + \widetilde{P_k} - D_k, & (3) \\ \dfrac{\partial \rho \omega}{\partial t} + \nabla(\rho u \omega) = \nabla(\Gamma_\omega \nabla \omega) + P_\omega - D_\omega + y_\omega, & (4) \end{cases}$$

with $\widetilde{P_k} = P_k - \beta \rho k \omega$ (where P_k and β are the volumetric production rate of k and a model constant, respectively). Γ_k and Γ_ω are the effective diffusivities for k and ω. D_k and D_ω are the turbulent dissipation terms, and y_ω is the cross-diffusion term in Equation (4). The k-ω SST model is extracted from the k-ϵ model using the following equation [42] to obtain the modified dissipation rate:

$$\omega = \frac{\epsilon}{k\, C_\mu}, \quad (5)$$

with C_μ a turbulence model coefficient. The knowledge of k and ω allows us to compute the turbulent viscosity.

In the numerical model, the computational time step was on the order of 10^{-3} s. For OpenFOAM, this time step varies to maintain a Courant number ([43]) less than 1. For all numerical simulations, the time step was constrained by the Courant–Friedrichs–Lewy (CFL) number, which ensures the numerical stability of the PIMPLE algorithm:

$$CFL = U_i \times \left| \frac{\Delta t}{\Delta x} \right| < 1, \tag{6}$$

where U_i is a free stream velocity in the i direction and Δt and Δx are the time step and the smallest cell length, respectively. Moreover, the time step can be fixed or variable. An adaptive time step was used here.

To validate the hydrodynamic model, the Root Mean Squared Error ($RMSE$) was computed as follows, as described by [44]:

$$RMSE = \sqrt{\frac{1}{n} \sum_{i=1}^{n} (\epsilon_i)^2}, \tag{7}$$

where n is the number observations. ϵ_i presents the difference between each observation and its measurement. However, relying only on the $RMSE$ for model reliability verification is not sufficient. Hence, the exploration of the R-squared error or coefficient of determination (R^2) was chosen for this purpose, which is expressed as follow:

$$R^2 = 1 - \frac{RMSE^2}{\sum_{i=1}^{n} (y_i - \bar{y})^2}, \tag{8}$$

with y_i representing the variable observations and $\bar{y}$ the mean value.

2.1.2. Boundary Conditions and Initial Conditions

For our study, the boundary conditions included no-slip conditions and Neumann boundary conditions. The no-slip condition was implemented with a wall law using the "nutkWallFunction", which provides an approximation of the turbulence properties in the near-wall region. This condition results in a zero velocity ($\vec{u} = 0$) near the wall, which signifies that the fluid particles in direct contact with a solid wall are effectively stationary relative to the wall's surface. Additionally, a homogeneous Neumann boundary condition was employed, which implies a zero velocity gradient ($\nabla \vec{u} = 0$).

Regarding the initial conditions, the inlet velocity conditions are expressed as follows:

$$\vec{u} = \begin{pmatrix} U_x \\ U_y \\ 0 \end{pmatrix} \times (\vec{X}\ \vec{Y}\ \vec{Z}), \tag{9}$$

with U_x and U_y the velocity components in the X and Y directions, respectively. For the turbulence intensity (I), a value of 5% was imposed throughout the initial domain. This value was based on the following equation [45]:

$$I = 0.16 \times Re^{-1/8}, \tag{10}$$

2.2. Lagrangian Model

2.2.1. Governing Equations

To simulate the larvae's dispersion, the Lagrangian numerical model Ichthyop [46] was used. Ichthyop is a modelling tool to assess how the physical and biological param-

eters influence the dynamics of the larvae, modelled using particles, by simulating their horizontal and vertical dispersion. It computes particle movements using ([47,48]):

$$\begin{cases} \dfrac{d\vec{P}_p}{dt} = \vec{u_p}, & (11) \\ \vec{u_p} = \vec{u} + \vec{v_s} + \vec{\mu_r}, & (12) \end{cases}$$

where $\vec{u_p}$ and $\vec{P}_p$ are the particle velocity and position, respectively. $\vec{v_s}$ and $\vec{\mu_r}$ are the settlement velocity and the velocity as a function of the time step and the horizontal diffusion. Ichthyop uses an advection numerical scheme based on the Runge–Kutta method (4th-order) for each time step after the interpolation of the velocity field. This advection scheme is efficient for computing the horizontal and vertical dispersion of the particles, as explained by [49]. Ichthyop, in its native form, operates without a mesh. The fundamental principle of Ichthyop is to receive input from a hydrodynamic model, which enforces the constraint of applying forcing on a structured grid.

2.2.2. Boundary Conditions and Initial Conditions

For each simulation, 10,000 particles were released at different depths in the case of one monopile or gravity-based foundations with two releases around and upstream of the foundation to represent the reef effect and the stepping-stone effect, respectively. In the case of two foundations with their actual positions' models, 100,000 particles were released on an area in front of the foundations depending on the current direction.

The initial time for a release was chosen relative to the onset of turbulent flow establishment near the foundation. Also, particles were considered as passive tracers without biological forcing, as the dispersion time was short compared to the actual larval phase.

2.3. Models' Coupling

To simulate larval dispersion, OpenFOAM fields on a regular mesh grid present the input data for Ichthyop (Figure 3). To achieve this, once the hydrodynamic model calculations are completed for all time steps, the results need to be interpolated onto a structured grid using linear interpolation (which seeks an approximation of the structured mesh for a regular grid) in order to be utilised as forcing data for Ichthyop. Ichthyop necessarily requires hydrodynamic model data on a structured grid as the input.

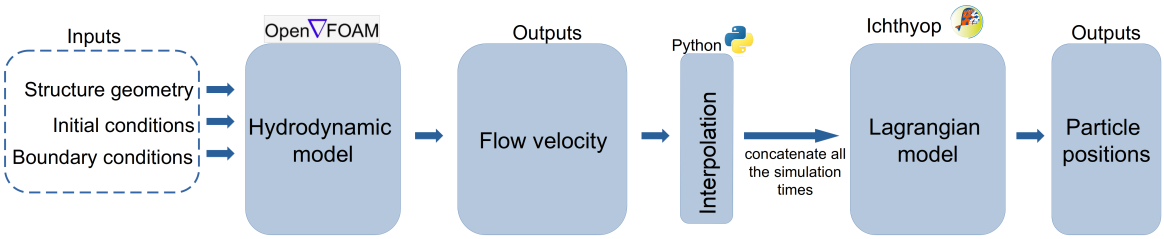

Figure 3. Coupling procedure to force Ichthyop by OpenFOAM fields.

3. A Laboratory Test Case

Our research focused on the interaction of flow currents with circular structures, a subject extensively explored in prior works, like [36]. This laboratory case served as a crucial validation test for our hydrodynamic model.

3.1. Domain Geometry

To validate our findings in this study, we replicated a domain configuration previously examined by [36] at a 1:10 scale (the scale choice is explained in Section 4), with dimensions of 36 m in length (L_R), 25 m in width (W_R), and 2.5 m in depth (H_R) (see Figure 4). To add

in this configuration, a 0.5 m-diameter cylinder was positioned 8 m away from the *X*-axis and 19.75 m from the *Y*-axis, as illustrated in Figure 4.

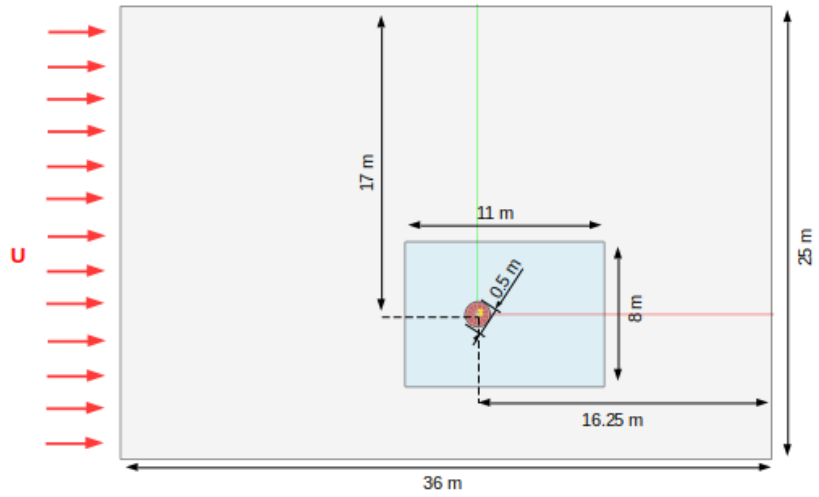

(**a**)

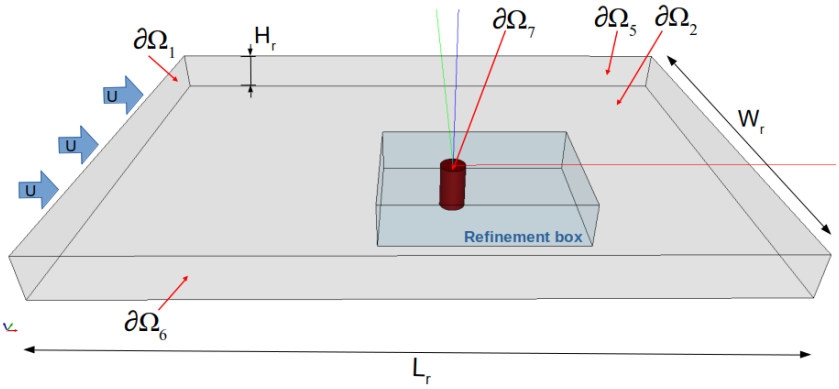

(**b**)

Figure 4. (**a**) Horizontal view (XY plane) of the experimental domain geometry (grey color) conducted by [36] at a 1:10 scale, including physical dimensions of the refinement box (blue color) and the pile (red color), along with inlet forcing (U). (**b**) The 3D view of the configuration domain with walls' definition.

As mentioned before, a 1:10 Froude scaling was applied. The numerical computations, requiring boundary and initial conditions, are described here (Figure 4). For the boundary conditions presented in Section 2, a no-slip condition ($\vec{u} = \vec{0}$) was applied on the lowerWall ($\partial\Omega_2$) for a flat bottom and on the pile ($\partial\Omega_7$). A homogeneous Neumann boundary condition ($\nabla\vec{u} = 0$) was applied on the outer edges of the domain referred to as the upperWall ($\partial\Omega_4$), back ($\partial\Omega_5$), and front ($\partial\Omega_6$). The flow was generated from the inlet ($\partial\Omega_1$) to the outlet ($\partial\Omega_3$) in the x direction with a uniform constant of velocity U_x applied as the initial condition and the same as the boundary condition. In this scenario of replicating the experiment conducted by [36], a variation of the velocity was imposed with 0.177 m/s and 0.31 m/s after applying the Froude similarity at a 1:10 scale to the real scale velocity of 0.6 m/s and 1 m/s, respectively.

3.2. Mesh

The mesh was characterised by uniformly sized cells across the entire domain, with a mesh size of $\Delta x = \Delta y = 0.1$ m. A ratio value of 0.5 between the horizontal and vertical mesh sizes was applied. In this case of the configuration, a refinement of level "2" around the foundation was implemented with an extension of 4 m upstream of the pile and 7 m

downstream, along the *X*-axis (see Figure 4). This approach aimed to concentrate more cells in the vicinity of the foundation, with different cell volumes from near the structure to the end of the domain (see Table 1 and Figure 5).

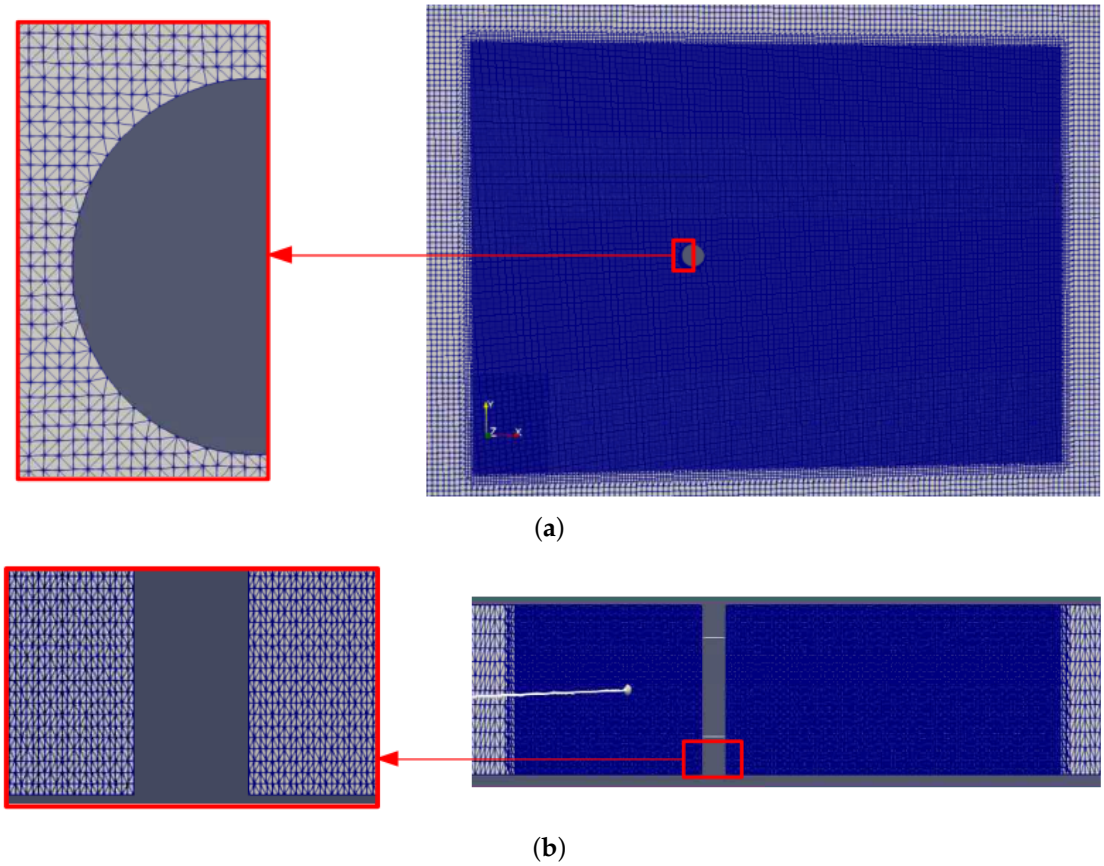

Figure 5. Refined mesh around the structure: (**a**) horizontal (XY plane) and (**b**) vertical (ZX plane).

Table 1. Mesh characteristics after refinement application.

	Monopile
Minimum cell volume (m^3)	1.6×10^{-5}
Maximum cell volume (m^3)	0.2×10^{-2}
Cell number	7,775,424
Point number	8,043,111

3.3. Results

In this section, a comparison was conducted between our numerical results and the experimental results conducted by [36] for the same configurations. Figure 6 shows that the Turbulent Kinetic Energy per unit (TKE) along the wake centerline downstream revealed a turbulence decrease with distance, showing a slight maximum gap of 1.4 $kg/m \cdot s^2$ between the measured and calculated values after 4 m (at a 1:10 scale) for the 0.31 m/s velocity case. For the 0.177 m/s velocity case, the TKE also showed a slight maximum gap of 0.58 $kg/m \cdot s^2$, which is illustrated in Figure 7. In both figures, the maximum phase shift occurred at $x = 6.25$ m, which is close to the refinement box limit and represents the point where the fluid transitions from a refined mesh to a coarser mesh. Beyond this point, the deviation remained nearly constant, as the turbulence stabilised and the mesh became regular. Regarding the deviation within the refinement box ($0 \leq x \leq 7$), it was minimal near the pile and began to increase, reaching a deviation of 1 $kg/m \cdot s^2$ for the 0.31 m/s

and 0.2 kg/m · s^2 for the 0.17 m/s velocity case at $x = 4$ m. This variable deviation within the refinement box was attributed to the structured mesh near the pile and the significant turbulence downstream. To analyse the accuracy of our results, the RMSE was calculated, which amounted to 0.76 kg/m · s^2 for the 0.31 m/s velocity case and 0.14 kg/m · s^2 for the 0.177 m/s velocity case, indicating that a faithful model should approach zero [44]. As highlighted in the preceding Section 2, relying solely on the RMS calculation is insufficient. Therefore, we incorporated the R^2 calculation to quantify the extent to which the mean value of the dependent variable was predicted by the independent variables. Referring to Equation (8), where y_i represents the TKE observations and $\bar{y}$ is the mean value, we obtained an R^2 value of 0.99 for the 0.177 m/s velocity case. For the 0.31 m/s velocity case, the R^2 value was close to 1, implying an almost perfect prediction of the experimental values based on our numerical model. This suggests that a significant portion of the variance in the mean value is explained by the model, indicating a strong fit.

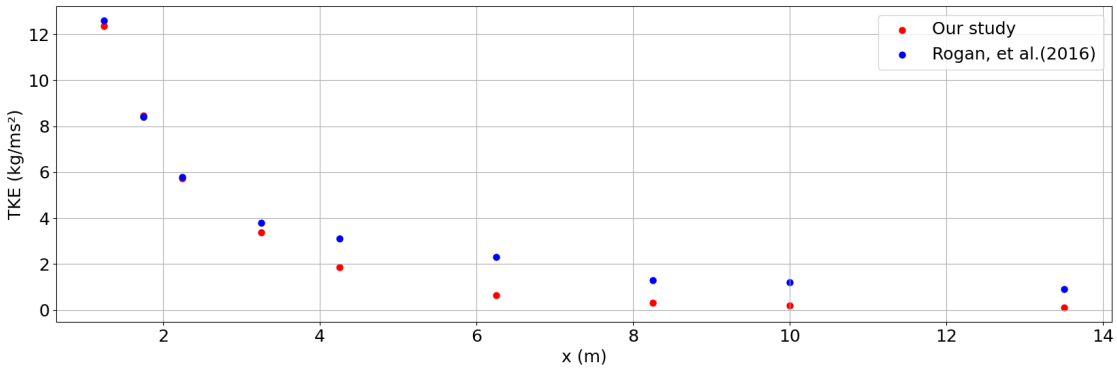

Figure 6. TKE values plotted against the distance from the structure along the *X*-axis at the water surface for the 0.31 m/s velocity case [36].

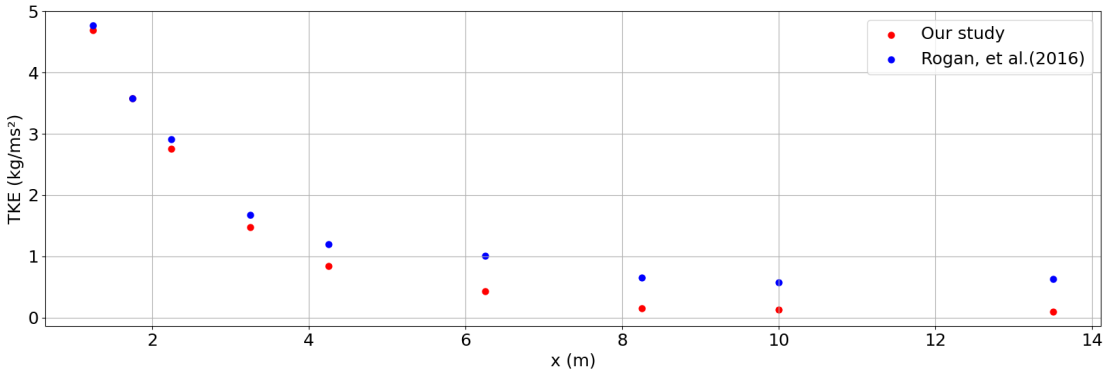

Figure 7. TKE values plotted against the distance from the structure along the *X*-axis at the water surface for the 0.177 m/s velocity case [36].

At 2.5D downstream of the pile, inside the refinement box, the TKE values for both velocities 0.31 m/s and 0.177 m/s showed a similar trend between our model and the experimental values. For this specific point shown in Figure 8, the normalised TKE value by the mean $\rho \bar{u_0}$ is provided for various y^* values (where $y^* = y/D$) within a layer at $x = 2.5D$. Whether for the two inlet velocities of 0.31 m/s or 0.177 m/s, the values were similar between the modelled and experimental data. The normalised TKE was highest along the wake's centerline and rapidly levelled off to a consistent background value on either side, for both our model and the experimental setup. The performance of the numerical model was evaluated for a transversal velocity comparison for initial velocities of 0.31 m/s and 0.177 m/s (Figure 8), using RMSE values of 6.82 $\times$ 10^{-5} kg/m $\times$ s^2 and

8.27×10^{-5} kg/m $\times$ s^2, respectively. Additionally, the numerical model fit the experimental data with an R^2 value of 0.99 for both velocity conditions.

These investigations demonstrated the capability of predicting the experimental results and highlight the influence of the proposed mesh.

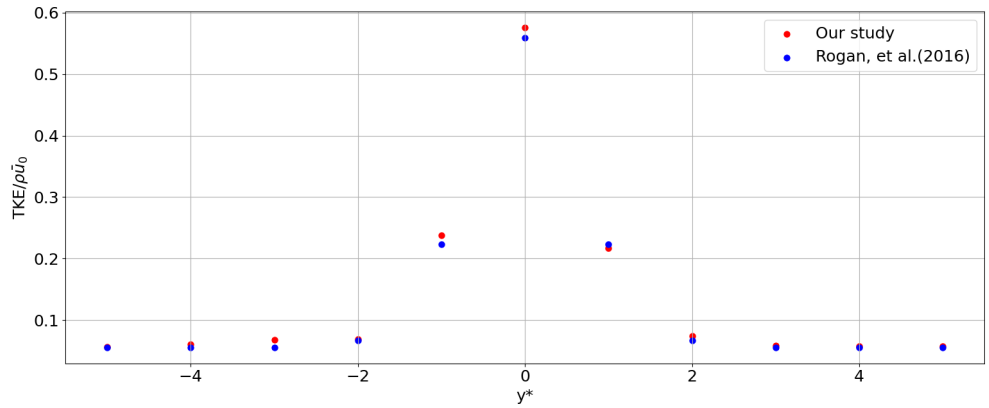

(**a**)

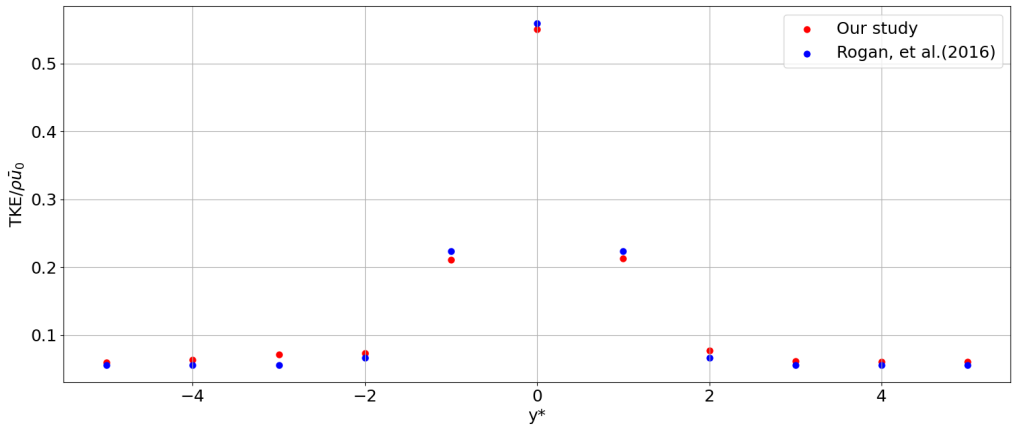

(**b**)

Figure 8. Normalised TKE values plotted against y* along the Y-axis for a cross-section at x = 2.5D downstream of the pile at the water surface for the (**a**) 0.31 m/s velocity case and (**b**) 0.177 m/s velocity case [36].

4. A Real Test Case

4.1. Domain Geometry

In this study, the requested computational resources were very important at a scale of 1, and therefore, the computation crashes. To work around this technical problem, a 1/10 scale was applied. After a Froude scaling at a 1:10 scale, we considered a domain length (L) of 130 m, a width (W) of 110 m, and a depth (H) of 3.28 m as average values used around a foundation of the OWFs of Courseulles-Sur-Mer and Fécamp (see Figure 9). The diameter of the vertical structure was $D = 0.65$ m for the monopile foundation. For the gravity-based foundation, a top diameter of $d_g = 0.73$ m and a base diameter $D_g = 3.2$ m were used, respecting the specifications of each OWF (see Figure 10). The structure was positioned in (x $= 0$, y $= 0$), leaving 20 m in front of the pile. In the two foundation cases and for the monopile, the computational domain length was 270 m, while the width was 114 m. The water depth was 3.28 m following the real positions of the foundations in the OWF of Courseulles-Sur-Mer. For an array of two gravity-based foundations, the dimensions of the computational domain were somewhat similar to the case of two monopile foundations

with a length of 240 m, a width of 84 m, and a water depth of 3.28 m, adding two structures located in the OWF of Fécamp. The boundaries of the computational domains were called $\partial\Omega_1$, $\partial\Omega_2$, $\partial\Omega_3$, $\partial\Omega_4$, $\partial\Omega_5$, and $\partial\Omega_6$ (Figure 9). The boundary of the structure was named $\partial\Omega_7$ for the two structures.

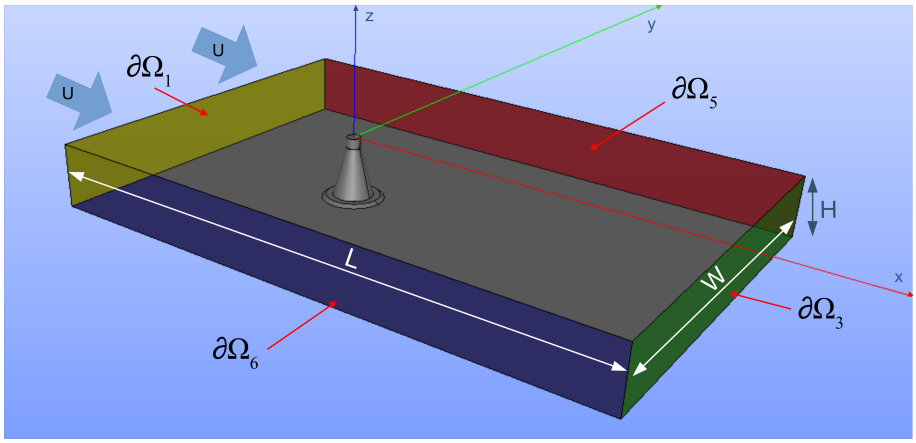

(**a**)

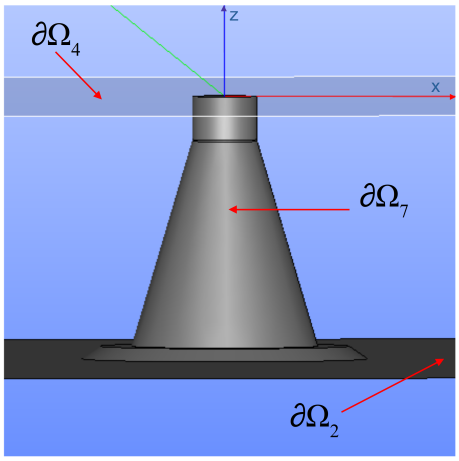

(**b**)

Figure 9. Geometry of the computational domain for the gravity-based foundation (drawn in grey) with boundaries: (**a**) 3D view and (**b**) 2D view (XZ plane).

For our configurations, the boundary walls are presented in Figure 9. For the boundary conditions, as the same methodology applied in the laboratory test case (Section 3), a no-slip condition ($\vec{u} = \vec{0}$) was applied on the lowerWall ($\partial\Omega_2$) for a flat bottom and on the structure ($\partial\Omega_7$). A homogeneous Neumann boundary condition ($\nabla\vec{u} = 0$) was applied on the outer edges of the domain, referred to as the upperWall ($\partial\Omega_4$), back ($\partial\Omega_5$), and front ($\partial\Omega_6$). The flow was generated from the inlet ($\partial\Omega_1$) to the outlet ($\partial\Omega_3$) in the x direction with a uniform constant of velocity U applied as the initial condition and the same as the boundary condition. This inlet velocity varied to simulate different hydrodynamic conditions. The values were set to 0.31 m/s, 0.18 m/s, and 0.03 m/s at a 1:10 scale for our study configurations. This is equal to 1 m/s; 0.6 m/s, and 0.1 m/s in real life, which represents strong, medium, and low tide-induced velocity in Courseulles-Sur-Mer.

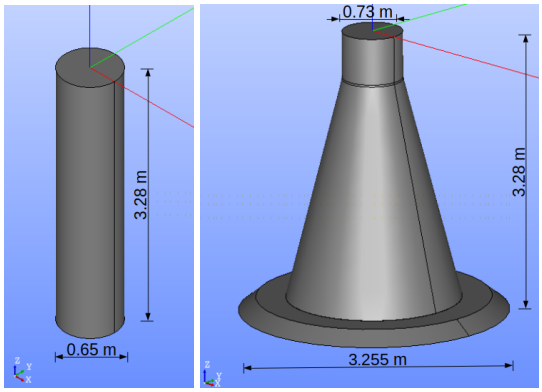

Figure 10. The 3D geometry with a 1:10 scale of the (**a**) monopile and (**b**) gravity-based structures.

4.2. Mesh

The mesh generator of OpenFOAM creates uniform mesh cells for the entire computational domain with a regular mesh size $\Delta x = \Delta y = 0.1$ m and $\Delta z = 0.205$ m. A ratio value of 0.5 between the horizontal and vertical mesh size was applied for the 1- or 2-foundation case, whether monopile or gravity-based. To ensure our model was accurate, we applied the same meshing technique for the model compared to the laboratory experiments by [36] analysed in Section 3. A refinement near the foundation was performed, which added supplementary layers and cells close to the foundation, keeping the same aspect ratio (see Figures 11 and 12) to capture small processes and strong velocity gradients. The mesh characteristics are summarised in Table 2.

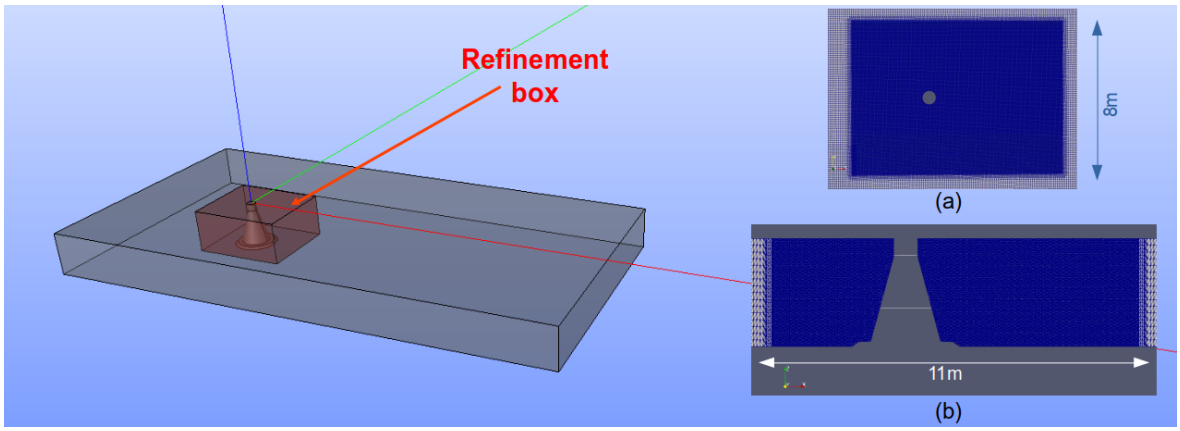

Figure 11. The 3D view of the mesh zones with the refinement box (red box) around the foundation (gravity-based structure). (**a**) Horizontal view (XY plane) of the refined mesh around the structure (grey colour) and (**b**) vertical view (ZX plane) of the refined mesh close to the foundation.

The results of our study were also compared to a mesh convergence study, which could enhance the simulations. To achieve this, the same domain/structure was applied with identical dimensions and positioning for the single monopile foundation case, employing the same refinement box dimensions, but at a lower refinement level, which decreased the number of cells and increased the minimum cell volume, as shown in Table 3. For our domains, the refinement was conducted at Level 2 (Figure 13b); hence, the meshed domain for the comparison was refined around the foundation at Level 1 (Figure 13a). For Level 1 and at 0.75 of the diameter upstream of the pile (-0.75D), there was a break in the mesh, as shown in Figure 13a.

Table 2. Mesh characteristics for monopile and gravity-based foundations in the case of one and two foundations.

	1 Foundation		2 Foundations	
	Monopile	**Gravity-Based**	**Monopile**	**Gravity-Based**
Minimum cell volume (m^3)	1.6×10^{-5}	1.57×10^{-5}	1.4×10^{-5}	0.6×10^{-5}
Maximum cell volume (m^3)	0.2×10^{-2}	0.2×10^{-2}	0.2×10^{-2}	0.2×10^{-2}
Cell number	31,802,304	31,655,500	73,859,440	56,285,086
Point number	33,455,002	33,307,259	77,483,496	58,829,361

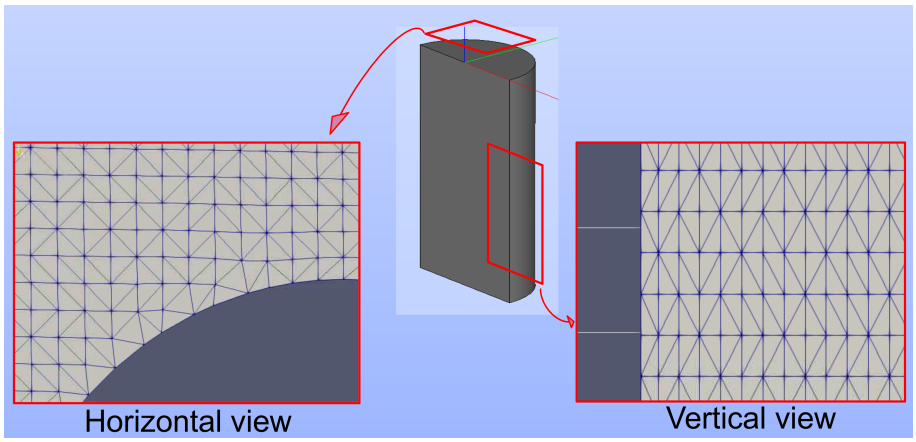

(**a**)

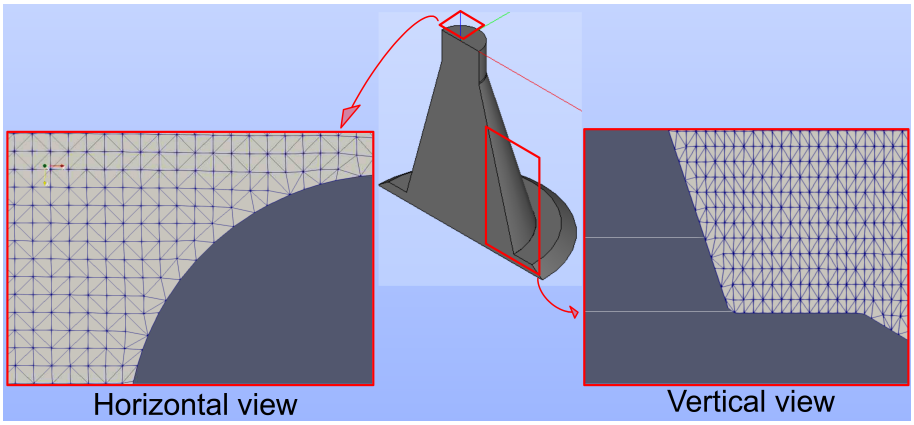

(**b**)

Figure 12. Zoom on the refined mesh around the structure: horizontal (XY plane, left panels) and vertical view (ZX plane, right panels) for (**a**) monopile and (**b**) gravity-based foundations.

Table 3. Mesh characteristics of the two configurations after refinement application with Level 1 and Level 2 meshing.

	Level 1	**Level 2**
Minimum cell volume (m^3)	1.3×10^{-4}	1.6×10^{-5}
Maximum cell volume (m^3)	0.2×10^{-2}	0.2×10^{-2}
Cell number	23,861,632	31,802,304
Point number	25,368,546	33,455,002

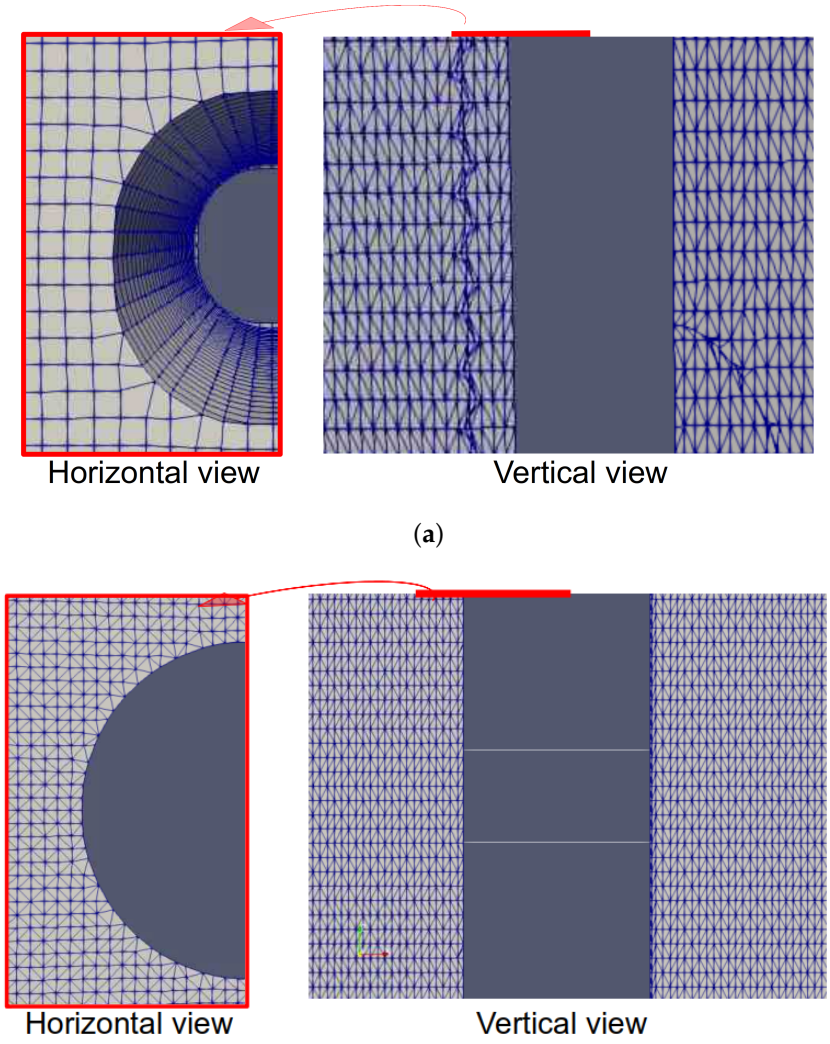

Figure 13. Zoom on the refined mesh around a monopile foundation: horizontal (XY plane) and vertical view (ZX plane) with (**a**) Level 1 and (**b**) Level 2 meshing. The distorted cells result from the cutting plane and do not accurately represent the 3D cells.

The velocity magnitude was compared within the refinement box located at one diameter behind the structure (Figure 14). At a distance of one diameter (1D) behind the structure, the turbulence effects were approximately 0.04 m/s weaker in the Level "1" fine meshing, which presented a coarser mesh configuration than our study configuration of Case "2". This phenomenon was attributed to the deformation of the fluid around the structure induced by the coarse mesh. Convergence was achieved between 2D and 3D with similar values for the two mesh levels. After three diameters from the pile (3D), there was a phase shift in the magnitude of the velocity values by approximately 0.02 m/s, which presented a 6.45% difference compared to the reference velocity value of 0.31 m/s, until the end of the refinement box located between 10D and 11D (Figure 14). At the point where the fluid exited the refined mesh (at 11D) in both configuration cases, it entered a regular mesh, which continued until the end of the domain. This explained the reduction in the phase difference observed for the magnitude between the two configurations, whether it be Level 1 or Level 2, hence the similarity in the magnitude value from 16D onwards further into the domain. The small difference in the value of approximately 4×10^{-3}, which presented a 1.29% difference compared to the reference velocity value, was attributed to the difference in the chosen point's position between the configurations. So, during this phase,

outside the refinement box, mesh convergence was achieved. To add to this, 20D represents only 20% of the domain downstream of the pile. These results and comparisons validated the chosen mesh and refinement type for ensuring the reliable reproduction of the fluid behaviour around the pile. The selection of this particular mesh configuration proved to be effective in accurately capturing the fluid dynamics in the vicinity of the stack.

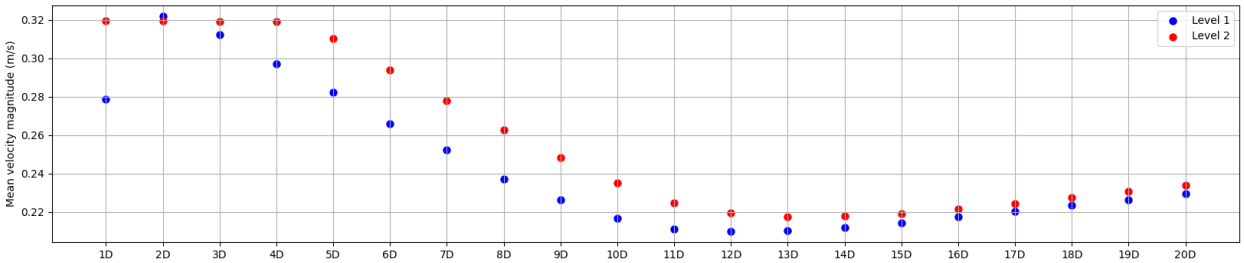

Figure 14. Mean velocity magnitude against the distance from the pile in terms of the Diameter (D) for the Level "1" (in blue) and Level "2" meshes (in red).

After the refined mesh with Level 2 in our case, we chose a variable time step. The CFL condition was satisfied in all hydrodynamic configurations for the monopile and gravity-based structures with one or two foundations. The CFL number varied between 0.2 and 0.7. The solver supports the adjustment of the time step based on the CFL number, as well as the relaxation of the transport equations to improve the performance. Despite the use of snappyHexMesh around the structures, the computation remained costly in terms of the computing time. For 1 h of simulation, more than 3.5 days of Central Processing Unit (CPU) time was required with 224 cores in the case of one foundation and more than 10 days of CPU time with 224 cores for two foundations.

4.3. Larvae Dispersion Simulations

For each simulation, 10,000 particles were released at different depths: at the surface, 1 m below the surface, 2 m below the surface, and at the bottom 3 m, below the water surface. In this study, two types of release were tested. In the first type of release, the spatial distribution of the particles had a circular shape of 0.65 m in diameter, located in the surface layer of 0.1 m in thickness and was 1 m from the front of the foundation (see Figure 15a). The other release type had a square shape distribution of particles around the foundation, adding one diameter around the pile (see Figure 15b). The release at the front represents particles that come from outside the domain (OWF), and the release around is the spread of particles that are already present around the foundation, initially from a reef effect on the structure, for example.

Moreover, particle dispersions were also applied for the case of a domain that contains two foundations. These simulation tests were implemented for two monopile foundations using a uniform current following the X-axis or an angle of $-20°$ from the X-axis. For the two gravity-based foundations, the inlet velocity deviated by 30° with respect to the X-axis. There would be 100,000 particles in those simulations, which would be released in an area in front of the foundations, depending on the current direction. The dispersion modelling in three dimensions used a time step of 0.015 s, and the particle positions were recorded every 2.5 s, which was the output time step of the hydrodynamic model. The initial time for a release was chosen relative to the onset of turbulent flow establishment near the foundation. According to the magnitude of the inlet velocity, the release time was determined following the ΔU value, defined such that:

$$\Delta U = |\vec{u}|_r - |\vec{u}|_y, \tag{13}$$

where $|\vec{u}|_r$ is the undisturbed velocity magnitude (Figure 16b, red point) and $|\vec{u}|_y$ is the near-foundation velocity magnitude (Figure 16b, green point). The steady state regime was easier to identify for the case of a gravity-based structure, so for the monopile structure case,

the same time for the release start was applied for both foundations to be able to compare the dynamics. The particles were considered as passive tracers without biological forcing.

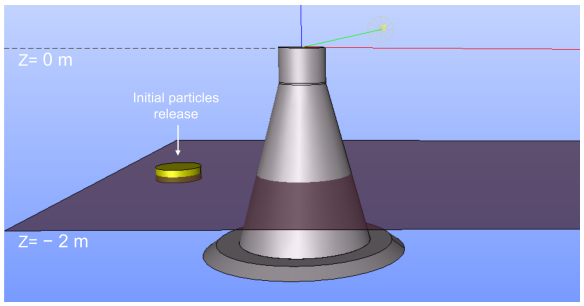

(**a**)

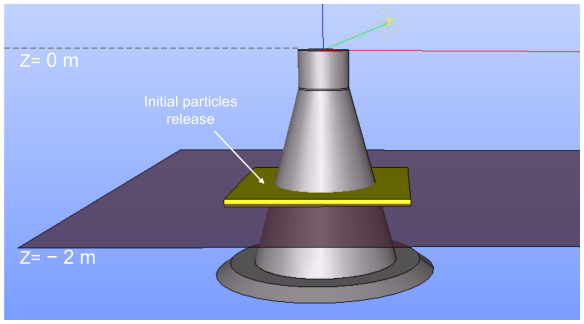

(**b**)

Figure 15. The 3D views of the initial particle releases (in yellow color) for two cases with an exemple at 2m under water surface: (**a**) in front of the foundation and (**b**) around the foundation.

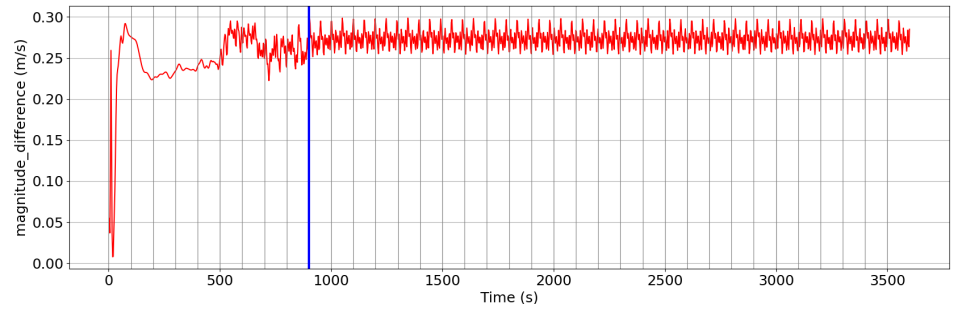

(**a**)

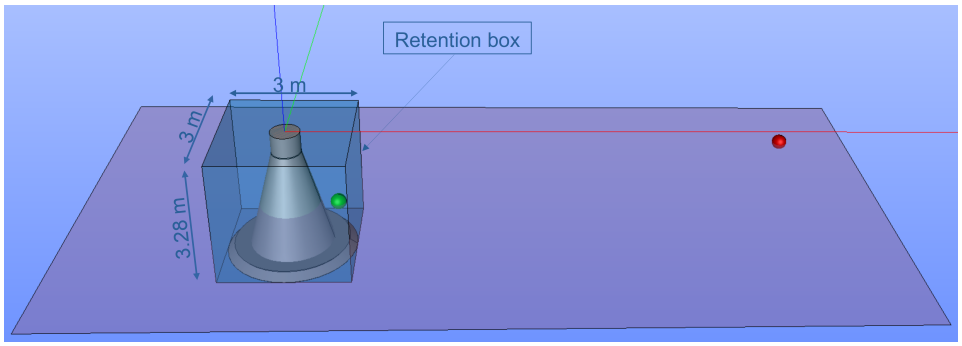

(**b**)

Figure 16. (**a**) Time evolution of ΔU for an inlet velocity of 0.31 m/s (red line). Initial time release (blue line) depending on the beginning of the steady state regime of the flow. (**b**) Location of $|\tilde{u}|_r$ (red point) and $|\tilde{u}|_y$ (green point) in the computational domain at 2 m below the surface and the retention box (blue box) dimensions around the foundation (in grey).

4.4. Coupling Procedure

An offline coupling between OpenFOAM and Ichthyop was carried out to simulate the larval dispersal (Figure 3).

The initial step involved running the OpenFOAM hydrodynamic model to obtain results for all time steps with an output time step of 2.5 s. The next step involved interpolating the OpenFOAM results onto a structured grid to achieve a regular grid using linear interpolation. This linear interpolation aimed to approximate the OpenFOAM mesh as closely as possible while preserving the same resolution. Defining a regular grid for Ichthyop is imperative. To simulate larval dispersion later on, Ichthyop uses OpenFOAM fields as the input data, using a regular mesh without including biological forcing and assuming passive particle movement (Figure 17).

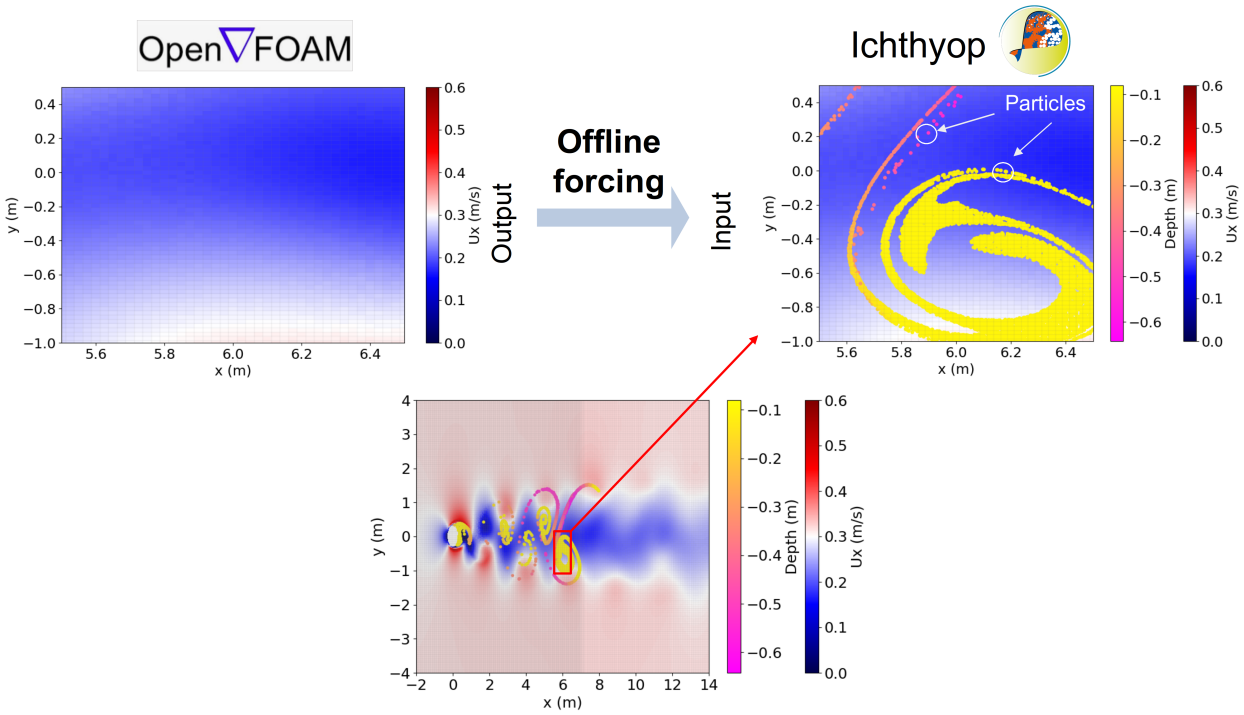

Figure 17. Conceptual scheme for the forcing of Ichthyop by the output of OpenFOAM. Zoom on a specific area (**top** row) and display of the entire domain (**bottom** row). Particles (yellow and pink dots) are superimposed over the X-velocity.

4.5. Results

4.5.1. General Hydrodynamics

The flow was examined thanks to the 2D views around the foundations (monopile and gravity-based). The Reynolds number (Re) being between 2×10^4 and 2×10^5, the hydrodynamic regime was, therefore, turbulent. As revealed by [50], at a high Re of (>5000), the turbulence was mainly induced by the von Kármán street vortices. von Kármán vortices create a periodic flow visible in the 2D visualisations of the vorticity and particle positions, as shown in Figure 18. These vortices present two symmetric turbulent shapes behind the pile, due to the alternative behaviour of the vortices.

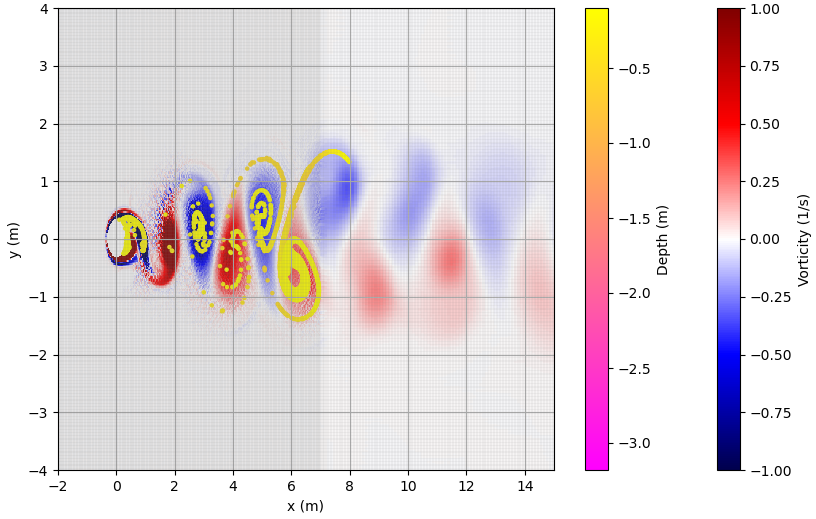

(**a**)

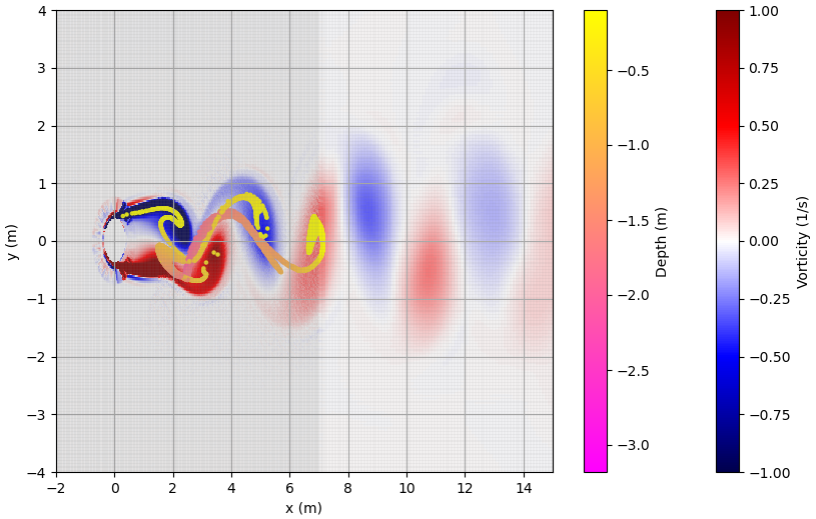

(**b**)

Figure 18. Horizontal view (XY plane) of the vorticity magnitude at the water surface layer with particles (dots coloured by depth position using a yellow–pink colour bar) after 30 s of release from the surface performed in front of the pile. Cases with (**a**) monopile and (**b**) gravity-based structure [51].

The von Kármán vortex shedding resulted in a number of vortices structured around the upstream of the pile, one of which is called the horseshoe vortex (see Figure 19; more details are given in [9,51]). For a near-bottom release of particles, this vortex, located near the bottom, forced the particles' motion by moving them upwards. This vertical movement was mainly induced by the negative values of the vertical velocity.

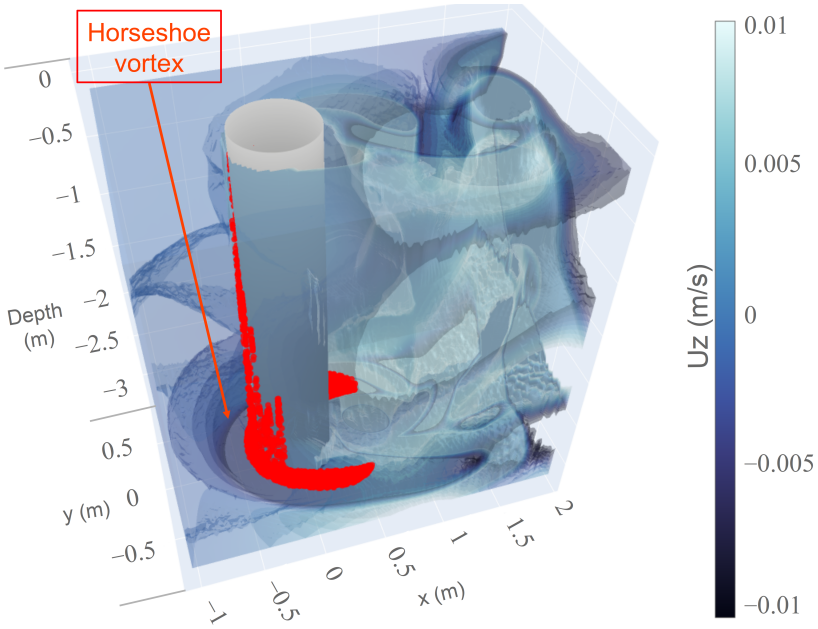

Figure 19. The 3D visualisation (x, y, depth) of the vertical velocity component (Uz) close to the monopile (light-grey cylinder) with particles (red dots).

To analyse the turbulent wake dynamics, the vortex shedding frequency (f) was calculated from the time period of the turbulent wake. To explain the regularity of this wake, the non-dimensional Strouhal number (St) [52] was calculated such that:

$$St = \frac{f \times h}{U}, \tag{14}$$

where h represents the pile diameter, which could be D, d_g, or D_g. This number represents the ratio between the advection time and the characteristic time of nonstationarity or vortex shedding. For a Re greater than 10^3 and for a circular cylinder, the St was about 0.2 [53]. Here, the Strouhal number value was found around 0.20 relying on the Re, as shown in Tables 4 and 5. The fluid forces the particles to be transported from below and out of the wake by the upward vortex and vice versa by the downward vortex.

Table 4. Monopile foundation: turbulence wake frequency (f), Strouhal number (St), and Reynolds number (Re) according to the magnitude of inlet velocity.

	U = 0.31 m/s	U = 0.18 m/s	U = 0.03 m/s
f	0.1	0.057	0.01
St	0.2	0.2	0.21
Re	2×10^5	1.2×10^5	1×10^4

Table 5. Same legend as for Table 4, but for a gravity-based foundation.

	U = 0.31 m/s	U = 0.18 m/s	U = 0.03 m/s
f (Hz)	0.08	0.05	0.008
St	0.19	0.2	0.195
Re	2.2×10^5	1.3×10^5	2.1×10^4

4.5.2. Sensitivity Tests

In this section, the retention time of the larvae, which were represented by particles, is studied according to the input velocity magnitude, type of foundation, and particle release location.

- **Effects of the Magnitude of Input Velocity**
  Using several input velocity values resulted in different retention times for particles to spread in three-dimensional space. To evaluate the sensitivity to the velocity value and initial release depth on larval dispersal, the retention time was found versus the percentage of particles that remained inside the retention box (3 m × 3 m × 3.28 m) around the foundations (see Figure 16b). The same size for the retention boxes was chosen for the monopile and gravity-based foundations. For each test, a retention time was calculated, which represents the period of time that the particles have remained close to the foundation inside the retention box until having 10% of the particles. As observed in Figures 20 and 21, the particle retention over time was slightly higher for the gravity-based structure than for the monopile foundation for every inlet velocity and depth release (see Tables 6 and 7). The longest retention time obtained for one foundation was about 9 min. This time was still much lower than the required time to have a real settlement around the structures. To add to this, the larval phase was between 3 weeks to 2 months for our study case, which took into account four benthic species (mussels, oysters, edible crabs, and Asian shore crabs) living in the Bay of Seine [54–57]. Hence, the longest retention time with $U = 0.03$ m/s and a release at 2 m below the water surface could be possible if considering particles coming from outside of the OWF and having already the competence to settle, depending the species.

Table 6. Retention time (10% threshold) for different input velocities and release depths in the case of a monopile foundation. (S − 0), (S − 1), (S − 2), and (S − 3) represent a release at the water surface, at 1 m, 2 m, and 3 m below the water surface, respectively.

	$U = 0.31$ m/s	$U = 0.18$ m/s	$U = 0.03$ m/s
$S - 0$	16 s	30 s	200 s
$S - 1$	17 s	33 s	200 s
$S - 2$	19 s	40 s	240 s
$S - 3$	18 s	33 s	220 s

Table 7. Same legend as for Table 6, but for a gravity-based foundation.

	$U = 0.31$ m/s	$U = 0.18$ m/s	$U = 0.03$ m/s
$S - 0$	40 s	45 s	335 s
$S - 1$	45 s	80 s	290 s
$S - 2$	55 s	115 s	540 s
$S - 3$	45 s	80 s	290 s

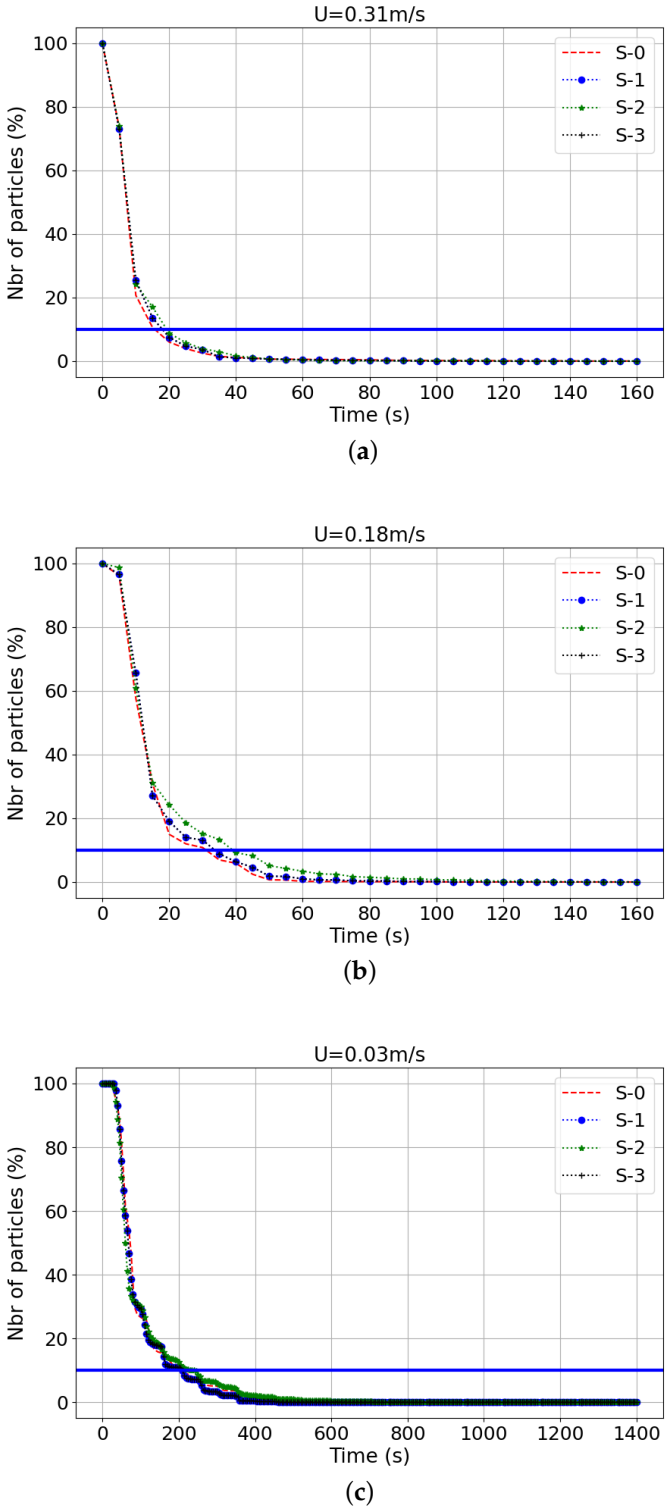

Figure 20. Time evolution of the number of particles (in percent) for a monopile and according to the release depth and input velocity magnitude: (**a**) $U = 0.31$ m/s, (**b**) $U = 0.18$ m/s and (**c**) $U = 0.03$ m/s. $(S-0)$, $(S-1)$, $(S-2)$, and $(S-3)$ represent a release at the water surface, at 1 m, 2 m, and 3 m below the water surface, respectively.

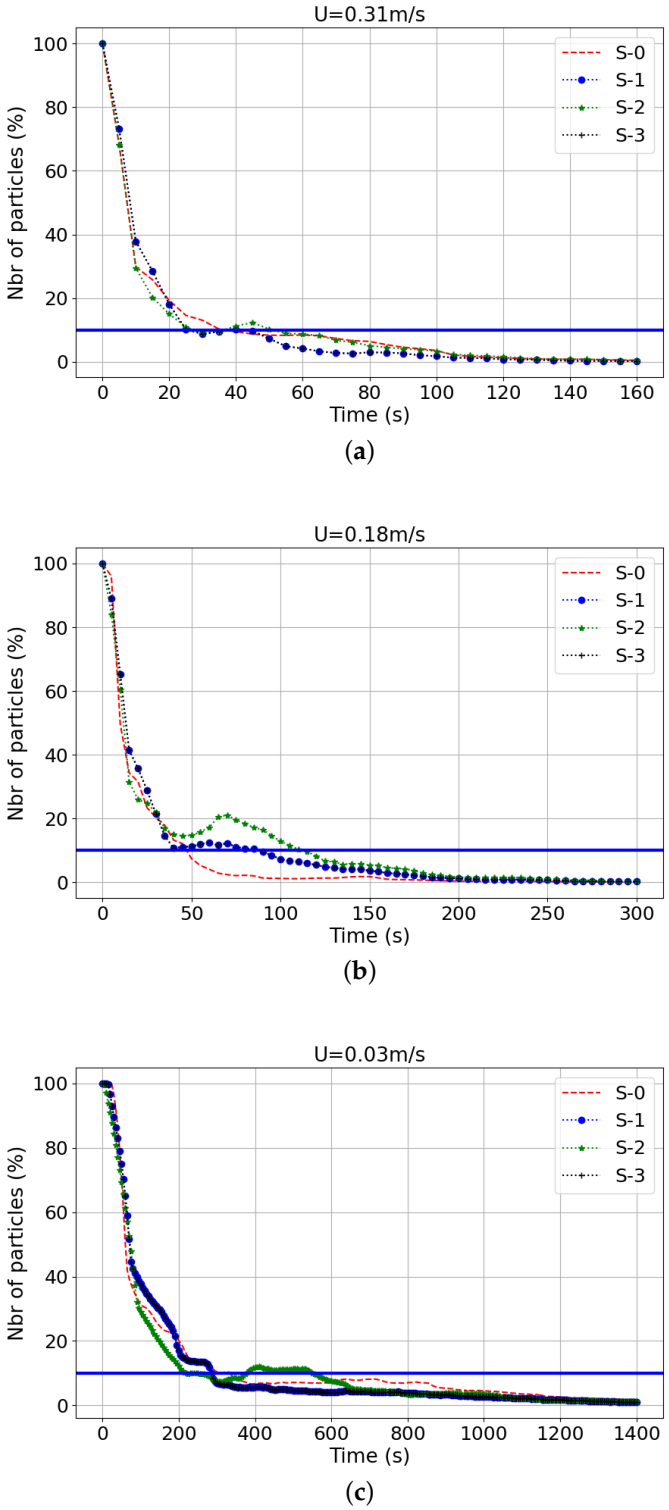

Figure 21. Same legend as for Figure 20, but for a gravity-based foundation.

- **Influence of the Type of Foundations**
  The structure–flow interaction generated a rhythmic flow past a circular cylinder, which can be affected by the vertical shape of the structure. In Figure 22, the vertical velocity related to the wake vortices is shown in the case of a release at 2 m below the surface and for a uniform inlet velocity equal to 0.31 m/s.

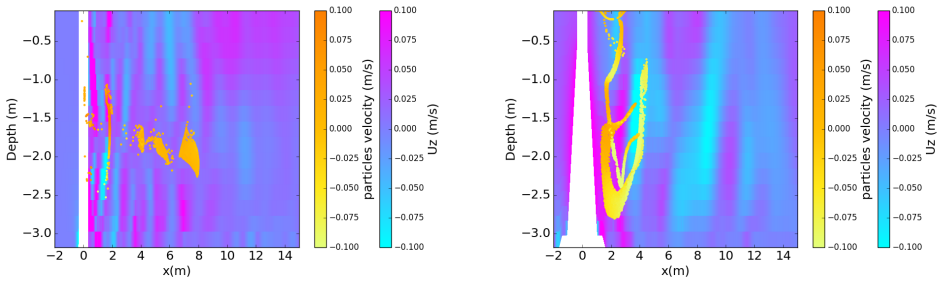

Figure 22. Vertical velocity Uz (XZ plane) (**a**) for monopile and (**b**) gravity-based (white structure) foundations with superimposed particles (green to orange dots) that have been released at 2 m under the water surface.

The vertical flow of wake vortices, as described by [9], drives the particle motions. The larval passive vertical velocity ultimately reflects a fluid force acting on the body motions. For a gravity-based foundation, particles had a faster vertical movement, probably the result of the conical large base (Figure 22) compared to a monopile foundation. To assess differences between the monopile and gravity-based foundations, a retention time was calculated for the gravity-based foundation for different initial depth releases around the structure and for several velocity values (see Tables 6 and 7). The intense vertical flow generated by the gravity-based foundation led to an increase in the retention time until 9 min against 4 min for a monopile foundation in the case of an input velocity of $U = 0.03$ m/s (see Table 8) and a release near the bottom (at 2 m below the water surface). There were no more larvae after 21 min in the retention box.

- **Impact of the Type of Release**
  This was almost similar in terms of the retention time versus the percentage of particles in the case of the monopile foundation, and a slight difference was observed in the case of the gravity-based foundation (see Figure 23). During the dispersion, there was a greater number of particles in the case where the initial release was behind the structure and for the gravity-based foundation. This result could be caused by the distance that the geometry of the structure took.

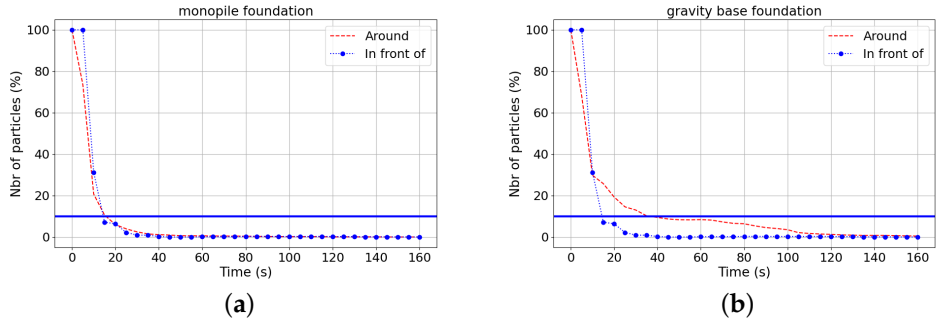

Figure 23. Time evolution of the number of particles for an input velocity of $U = 0.31$ m/s and for: (**a**) monopile foundation release at water surface performed in front of (blue dotted line with circles) and around (red dashed line) the structures; (**b**) same type of release as for (**a**), but for a gravity-based foundation.

Table 8. Retention time (10% threshold) for $U = 0.31$ m/s and $U = 0.03$ m/s according to different release types (around and in front of the structure) and for the two foundations.

	Monopile		Gravity-Based	
	In Front of	**Around**	**In Front of**	**Around**
$U = 0.31$ m/s	14 s	15 s	14 s	40 s
$U = 0.03$ m/s	190 s	200 s	480 s	335 s

4.6. Case of an Array of Foundations

In this part, the presence of a second foundation on larval dispersal was evaluated. The impact on the particle retention times in the vicinity of the second foundation was investigated in particular. The flow was computed using $U = 0.31$ m/s, which represents a spring tide event for Courseulles-Sur-Mer [5] and adding an angle at $-20°$ in the flow direction from the X-axis. The same input velocity was applied for Fécamp (i.e., gravity-based foundation), but with a deviation of 30° from the X-axis. A similar vorticity pattern was observed for the two foundations (Figure 24).

The dispersal was simulated from the input wall of the computational domain as the initial particle release. We studied the influence of the presence of an array of foundations on the larvae's dispersion near the second structure. In Table 9, the number of particles over time was attributed based on the particles that entered the retention box, located around the second foundation. Particles near the second foundation were only trapped for the gravity-based foundation case due to its geometry. In Figure 24, the vertical velocity is negative close to the bottom near the conical area, which resulted in a downward flow, which maintained the particles in this area. Thus, no particles were attached for the monopile structures.

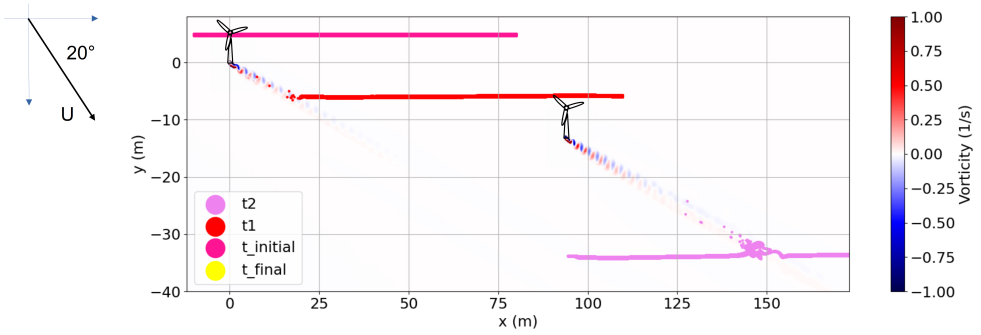

(**a**)

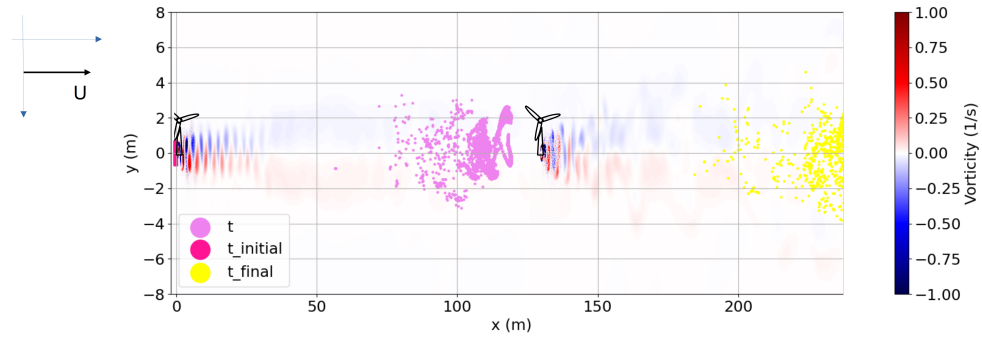

(**b**)

Figure 24. *Cont.*

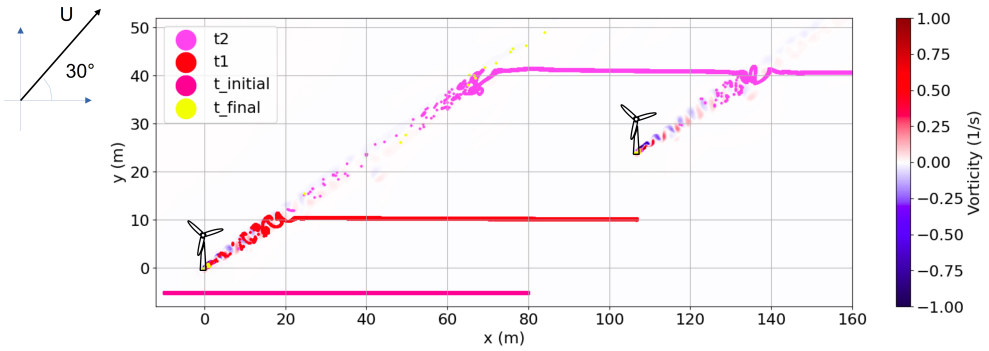

Figure 24. Horizontal view (XY plane) of the fluid vorticity (blue–red colours) around two foundations with particle positions drawn at different times (t or t_1 and t_2 are the intermediate times; $t_{initial}$ is the initial time; t_{final} is the final time). For the (**a**) monopile case (Courseulles-Sur-Mer OWF) with an input velocity oriented to the southeast, (**b**) monopile case (Courseulles-Sur-Mer OWF) with an input velocity oriented to the east, and (**c**) gravity-based case (Fécamp OWF) with an input velocity oriented to the northeast. Black wind turbines represent the foundations.

Table 9. Number of settled particles in the vicinity of the second foundation according to the direction of the inlet velocity and type of foundation.

	No. of Settled Particles (%)
Monopile ($\theta = 0°$)	0
Monopile ($\theta = -20°$)	0
Gravity-based ($\theta = 30°$)	0.4

4.7. Assessment of a Possible Reef Effect or Stepping-Stone Effects

For all simulations, the larvae were considered as totally passive in the water column. We assumed that the passive deposition hypothesis [58] can be applied to provide the settlement of the larvae of bentho-pelagic species near the OWF. In her review, Butman [58] highlighted that some bivalve larvae may result from passive accumulation in sheltered or weak current areas. The author also highlighted the potential importance of strong near-bed currents for maintaining larvae in suspension. Otherwise, weak currents are shown to allow the settlement of particles on the sea bottom. The trapping of particles near the bottom, as observed here (Figure 19), supports this conclusion. The fall velocities of larvae were estimated to be between 1.5×10^{-4} m/s and 3×10^{-3} m/s. This is slightly smaller than the fall velocities found in this study, which varied between 3×10^{-4} and 3×10^{-2} m/s (see Figure 22). The near-bottom current speed ranged from 0 to 0.2 m/s at a distance of 0.5 m above the bottom, while it was from 0 to 0.31 m/s here. The time that larvae choose a preferred habitat within a fluid flow remains unknown.

5. Conclusions

The objective of this study was to explore the effects of the magnitude and direction of flow velocity, foundation type, release type, and an array of foundations on the retention time of particles near the structure to help the development of wind energy at sea. This work is innovative in that it provided estimates of the retention times under different conditions and for 3D cases. Such times are useful to evaluate the OWF's impacts on connectivity. In terms of hydrodynamics, fluid–structure interaction generates horseshoe vortices near the bottom of the foundation due to the vertical shedding. The main flow features involve von Kármán vortices with upward and downward motions and turbulent wakes and stresses, as observed in the 3D numerical simulations. The inlet velocity magnitude influences the retention time of particles: the lower is the velocity, the higher is the retention time. By

decreasing the velocity from 0.31 m/s to 0.03 m/s, the retention time increases by 183 s for the monopile foundation and by 245 s for the gravity-based foundation. One of the other main findings was that the gravity-based foundation, due to its particular geometry, increased the intensity of the vertical transport of the particles in comparison to the monopile foundation. A similar particle number transported using different initial release types for the monopile foundation was found, for example in the case of a velocity of 0.31 m/s, there were 14 s of retention time with the initial release in front of the foundation versus 15 s in the case of the initial release around the foundation. For the gravity-based foundation, the retention time between the initial release position was slightly different with 26 s as the difference between the in front of and around releases with the velocities equal to U = 0.31 m/s and 145 s as the difference between the two releases types with a velocity U = 0.03 m/s. For the sensitivity tests with two foundations, there were fewer particles over less retention time for the second monopile foundation in the case of a uniform velocity. All those findings were valid only for a constant inlet velocity (and for high Reynolds numbers), a flat bottom, and similar geometries and meshes. It is not possible to simulate an entire OWF for the moment due to our limited computational resources. In the same spirit, the inclusion of wave, wind, and sediment effects remains difficult for the same technical reasons as it would involve using a three-phase solver (air–water–sediment) in OpenFOAM.

Future works will be focused on the impact of OWFs on larval dispersal at a regional scale (for monopile and gravity-based foundations), by coupling the Model for Applications at Regional Scale (MARS3D) ocean circulation model with the Lagrangian model Ichthyop using appropriate parametrisations and adding biological forcing. The numerical results will be compared with in situ observations at a 1:1 scale in terms of hydrodynamics and larval concentration. This regional-scale study will allow exploring the influence of an entire OWF under met-ocean forcings (tide/wind) on larval dispersal and investigate the role of the OWF in the connectivity of benthic-pelagic species in the extended Bay of Seine.

Author Contributions: Methodology, S.A., M.B. and A.-C.B.; Software, S.A. and M.B.; Validation, S.A., A.-C.B., J.-C.D. and J.-P.P.; Investigation, S.A.; Data curation, M.B.; Writing—original draft, S.A.; Writing—review & editing, M.B., A.-C.B., J.-C.D. and J.-P.P.; Supervision, M.B., A.-C.B. and J.-C.D.; Project administration, A.-C.B.; Funding acquisition, A.-C.B. and J.-C.D. All authors have read and agreed to the published version of the manuscript.

Funding: This research was funded by Region Normandy, the Agency for the Environment and Energy Management (ADEME) and by University of Caen Normandy, through a PhD grant (no grant number).

Institutional Review Board Statement: Not applicable.

Informed Consent Statement: Not applicable.

Data Availability Statement: The authors will provide OpenFoam and Ichthyop files and result data on request.

Acknowledgments: This work is a part of a thesis financed by Region Normandy and the Agency for the Environment and Energy Management (ADEME). The present work was carried out using the computing resources of Regional Computer Center and Digital Applications of Normandy (CRIANN) (Normandy, France). The researches have benefited from the Continental and Coastal Morphodynamics (M2C, CNRS) laboratory facilities.

Conflicts of Interest: The funders had no role in the design of the study; in the collection, analyses, or interpretation of data; in the writing of the manuscript; or in the decision to publish the results.

References

1. Aminoroayaie Yamini, O.; Mousavi, S.H.; Kavianpour, M.R.; Movahedi, A. Numerical modelling of sediment scouring phenomenon around the offshore wind turbine pile in marine environment. *Environ. Earth Sci.* **2018**, *77*, 776. [CrossRef]
2. Díaz, H.; Soares, C.G. Review of the current status, technology and future trends of offshore wind farms. *Ocean Eng.* **2020**, *209*, 107381. [CrossRef]
3. Sánchez, S.; López-Gutiérrez, J.S.; Negro, V.; Esteban, M.D. Foundations in offshore wind farms: Evolution, characteristics and range of use. Analysis of main dimensional parameters in monopile foundations. *J. Mar. Sci. Eng.* **2019**, *7*, 441. [CrossRef]

4. Lavanya, C.; Kumar, N.D. Foundation Types for Land and Offshore Sustainable Wind Energy Turbine Towers. *E3S Web Conf.* **2020**, *184*, 01094. [CrossRef]
5. Rivier, A.; Bennis, A.C.; Pinon, G.; Magar, V.; Gross, M. Parameterization of wind turbine impacts on hydrodynamics and sediment transport. *Ocean Dyn.* **2016**, *66*, 1285–1299. [CrossRef]
6. Pezy, J.P.; Dauvin, J.C. Wide coverage but few quantitative data: Coarse sediments in the English Channel. *Ecol. Indic.* **2021**, *121*, 107010. [CrossRef]
7. Méar, Y.; Poizot, E.; Murat, A.; Beryouni, K.; Baux, N.; Dauvin, J.C. Improving the monitoring of a dumping site in a dynamic environment. Example of the Octeville site (Bay of Seine, English Channel). *Mar. Pollut. Bull.* **2018**, *129*, 425–437. [CrossRef]
8. Clark, S.; Schroeder, F.; Baschek, B. *The Influence of Large Offshore Wind Farms on the North Sea and Baltic Sea: A Comprehensive Literature Review*; Helmholtz-Zentrum Geesthacht, Zentrum für Material-und Küstenforschung: Geesthacht, Germany, 2014.
9. Petersen, T.U.; Sumer, B.M.; Fredsøe, J.; Raaijmakers, T.C.; Schouten, J.J. Edge scour at scour protections around piles in the marine environment—Laboratory and field investigation. *Coast. Eng.* **2015**, *106*, 42–72. [CrossRef]
10. Christensen, E.D.; Johnson, M.; Sørensen, O.R.; Hasager, C.B.; Badger, M.; Larsen, S.E. Transmission of wave energy through an offshore wind turbine farm. *Coast. Eng.* **2013**, *82*, 25–46. [CrossRef]
11. Wieselsberger, C. New data on the laws of fluid resistance. *Phys. Z.* **1922**, *22*, 321–328.
12. Thom, A. The flow past circular cylinders at low speeds. *Proc. R. Soc. Lond. A* **1933**, *141*, 651–669.
13. Homann, F. Einfluß großer zähigkeit bei strömung um zylinder. *Forschung auf dem Gebiet des Ingenieurwesens A* **1936**, *7*, 1–10. [CrossRef]
14. Sarpkaya, T. *Vortex Shedding and Resistance in Harmonic Flow about Smooth and Rough Circular Cylinders at High Reynolds Numbers*; Technical Report; Naval Postgraduate School: Monterey, CA, USA, 1976.
15. Kawamura, T.; Hiwada, M.; Hibino, T.; Mabuchi, I.; Kumada, M. Flow around a finite circular cylinder on a flat plate: Cylinder height greater than turbulent boundary layer thickness. *Bull. JSME* **1984**, *27*, 2142–2151. [CrossRef]
16. Eckerle, W.A.; Langston, L. Horseshoe vortex formation around a cylinder. *J. Turbomach.* **1987**, *109*, 278–285. [CrossRef]
17. Sumer, B.M.; Fredsøe, J. Scour at the head of a vertical-wall breakwater. *Coast. Eng.* **1997**, *29*, 201–230. [CrossRef]
18. Williamson, C. Three-dimensional wake transition. *J. Fluid Mech.* **1996**, *328*, 345–407. [CrossRef]
19. Fredsoe, J.; Sumer, B.M. *Hydrodynamics around Cylindrical Structures*, Revised ed.; World Scientific Publishing Company: Singapore, 2006; Volume 26.
20. Zhang, H.Q.; Fey, U.; Noack, B.R.; König, M.; Eckelmann, H. On the transition of the cylinder wake. *Phys. Fluids* **1995**, *7*, 779–794. [CrossRef]
21. Orszag, S.A. Analytical theories of turbulence. *J. Fluid Mech.* **1970**, *41*, 363–386. [CrossRef]
22. Wilcox, D.C. Reassessment of the scale-determining equation for advanced turbulence models. *AIAA J.* **1988**, *26*, 1299–1310. [CrossRef]
23. Menter, F.R. Two-equation eddy-viscosity turbulence models for engineering applications. *AIAA J.* **1994**, *32*, 1598–1605. [CrossRef]
24. Celik, I.; Shaffer, F.D. Long time-averaged solutions of turbulent flow past a circular cylinder. *J. Wind Eng. Ind. Aerodyn.* **1995**, *56*, 185–212. [CrossRef]
25. Khan, N.B.; Ibrahim, Z. Numerical investigation of vortex-induced vibration of an elastically mounted circular cylinder with One-degree of freedom at high Reynolds number using different turbulent models. *Proc. Inst. Mech. Eng. Part M J. Eng. Marit. Environ.* **2019**, *233*, 443–453. [CrossRef]
26. Planes, S.; Parroni, M.; Chauvet, C. Evidence of limited gene flow in three species of coral reef fishes in the lagoon of New Caledonia. *Mar. Biol.* **1998**, *130*, 361–368. [CrossRef]
27. Dannheim, J.; Bergström, L.; Birchenough, S.N.; Brzana, R.; Boon, A.R.; Coolen, J.W.; Dauvin, J.C.; De Mesel, I.; Derweduwen, J.; Gill, A.B.; et al. Benthic effects of offshore renewables: Identification of knowledge gaps and urgently needed research. *ICES J. Mar. Sci.* **2020**, *77*, 1092–1108. [CrossRef]
28. Van Berkel, J.; Burchard, H.; Christensen, A.; Mortensen, L.O.; Petersen, O.S.; Thomsen, F. The effects of offshore wind farms on hydrodynamics and implications for fishes. *Oceanography* **2020**, *33*, 108–117. [CrossRef]
29. Nicolle, A.; Dumas, F.; Foveau, A.; Foucher, E.; Thiébaut, E. Modelling larval dispersal of the king scallop (*Pecten maximus*) in the English Channel: Examples from the bay of Saint-Brieuc and the bay of Seine. *Ocean. Dyn.* **2013**, *63*, 661–678. [CrossRef]
30. Adams, T.P.; Miller, R.G.; Aleynik, D.; Burrows, M.T. Offshore marine renewable energy devices as stepping stones across biogeographical boundaries. *J. Appl. Ecol.* **2014**, *51*, 330–338. [CrossRef]
31. Greifzu, F.; Kratzsch, C.; Forgber, T.; Lindner, F.; Schwarze, R. Assessment of particle-tracking models for dispersed particle-laden flows implemented in OpenFOAM and ANSYS FLUENT. *Eng. Appl. Comput. Fluid Mech.* **2016**, *10*, 30–43. [CrossRef]
32. Floeter, J.; van Beusekom, J.E.; Auch, D.; Callies, U.; Carpenter, J.; Dudeck, T.; Eberle, S.; Eckhardt, A.; Gloe, D.; Hänselmann, K.; et al. Pelagic effects of offshore wind farm foundations in the stratified North Sea. *Prog. Oceanogr.* **2017**, *156*, 154–173. [CrossRef]
33. Pothin, K. Analyse de la Dispersion Larvaire des Poissons Récifaux à la Réunion à Travers l'étude de Leurs Otolithes. Ph.D. Thesis, Université de La Réunion, Saint-Denis, France, 2005.
34. Esteban, M.D.; López-Gutiérrez, J.S.; Negro, V. Gravity-based foundations in the offshore wind sector. *J. Mar. Sci. Eng.* **2019**, *7*, 64. [CrossRef]
35. Wu, X.; Hu, Y.; Li, Y.; Yang, J.; Duan, L.; Wang, T.; Adcock, T.; Jiang, Z.; Gao, Z.; Lin, Z.; et al. Foundations of offshore wind turbines: A review. *Renew. Sustain. Energy Rev.* **2019**, *104*, 379–393. [CrossRef]

36. Rogan, C.; Miles, J.; Simmonds, D.; Iglesias, G. The turbulent wake of a monopile foundation. *Renew. Energy* **2016**, *93*, 180–187. [CrossRef]
37. Greenshields; Christopher. *OpenFOAM User Guide*; OpenFOAM Found. Ltd Version; The OpenFOAM Foundation: London, UK, 2015; Volume 3, p. 47.
38. Issa, R.I. Solution of the implicitly discretised fluid flow equations by operator-splitting. *J. Comput. Phys.* **1986**, *62*, 40–65. [CrossRef]
39. Patankar, S.V.; Spalding, D.B. A calculation procedure for heat, mass and momentum transfer in three-dimensional parabolic flows. *Int. J. Heat Mass Transf.* **1983**, *1*, 54–73.
40. Aravind Karthik, M.; Srinivas, G.; Naik, N. Implementation of Higher-Order PIMPLE Algorithm for Time Marching Analysis of Transonic Wing Compressibility Effects with High Mach Pre-Conditioning. *Eng. Sci.* **2022**, *20*, 218–235.
41. Liu, Y.; Xiao, Q.; Incecik, A.; Peyrard, C.; Wan, D. Establishing a fully coupled CFD analysis tool for floating offshore wind turbines. *Renew. Energy* **2017**, *112*, 280–301. [CrossRef]
42. Wilcox, D.; Traci, R. A complete model of turbulence. In Proceedings of the 9th Fluid and PlasmaDynamics Conference, San Diego, CA, USA, 14–16 July 1976; p. 351.
43. Courant, R.; Friedrichs, K.; Lewy, H. Uber die Differenzengleichungen der Mathematischen Physik. *Math. Ann.* **1928**, *100*, 32. [CrossRef]
44. Gy, P. *Sampling for Analytical Purposes*; John Wiley & Sons: Hoboken, NJ, USA, 1998.
45. Manual, U. *ANSYS FLUENT 12.0*; Theory Guide; ANSYS Inc.: Cannonsburg, PA, USA. 2009. Available online: https://www.afs.enea.it/project/neptunius/docs/fluent/html/th/main_pre.htm (accessed on 7 November 2023).
46. Lett, C.; Verley, P.; Mullon, C.; Parada, C.; Brochier, T.; Penven, P.; Blanke, B. A Lagrangian tool for modelling ichthyoplankton dynamics. *Environ. Model. Softw.* **2008**, *23*, 1210–1214. [CrossRef]
47. Davidson, F.J.; Deyoung, B. Modelling advection of cod eggs and larvae on the Newfoundland Shelf. *Fish. Oceanogr.* **1995**, *4*, 33–51. [CrossRef]
48. Collins, C.; Hermes, J. Modelling the accumulation and transport of floating marine micro-plastics around South Africa. *Mar. Pollut. Bull.* **2019**, *139*, 46–58. [CrossRef]
49. Peliz, A.; Marchesiello, P.; Dubert, J.; Marta-Almeida, M.; Roy, C.; Queiroga, H. A study of crab larvae dispersal on the Western Iberian Shelf: Physical processes. *J. Mar. Syst.* **2007**, *68*, 215–236. [CrossRef]
50. Norberg, C. *Effects of Reynolds Number and a Low-Intensity Freestream Turbulence on the Flow around a Circular Cylinder*; Chalmers University of Technology: Gothenburg, Sweden, 1987; Volume 87, pp. 1–55.
51. Ajmi, S.; Boutet, M.; Bennis, A.C.; Pezy, J.P.; Dauvin, J.C. Impact of the turbulent wake downstream offshore wind turbines on larval dispersal. *Trends Renew. Energ. Offshore* **2022**, *10*, 3–8.
52. Strouhal, V. Über eine besondere Art der Tonerregung. *Ann. Phys.* **1878**, *24*, 216251.
53. Blevins, R.D. *Flow-Induced Vibration*; Van Nostrand Reinhold Company: New York, NY, USA, 1977.
54. Toupoint, N.; Mohit, V.; Linossier, I.; Bourgougnon, N.; Myrand, B.; Olivier, F.; Lovejoy, C.; Tremblay, R. Effect of biofilm age on settlement of Mytilus edulis. *Biofouling* **2012**, *28*, 985–1001. [CrossRef]
55. His, E.; Robert, R. Developpement des veligeres de Crassostrea gigas dans le bassin d'Arcachon. Etudes sur les mortalites larvaires. *Rev. Trav. De l'Institut Pêches Marit.* **1983**, *47*, 63–88.
56. Bennett, D.B. Factors in the life history of the edible crab (*Cancer pagurus* L.) that influence modelling and management. *Ices Mar. Sci. Symp.* **1995**, *199*, 89–98.
57. Epifanio, C.E. Invasion biology of the Asian shore crab Hemigrapsus sanguineus: A review. *J. Exp. Mar. Biol. Ecol.* **2013**, *441*, 33–49. [CrossRef]
58. Butman, C. Larval settlement of soft-sediment invertebrates: The spatial scales of pattern explained by active habitat selection and the emerging role of hydrodynamical processes. *Oceanogr. Mar. Biol.* **1987**, *25*, 113–165.